

# **Fiber Fabry-Perot Cavities for Quantum Information and Spectroscopy**

David Röser

Masterarbeit in Physik  
angefertigt im Institut für Angewandte Physik

vorgelegt der  
Mathematisch-Naturwissenschaftlichen Fakultät  
der  
Rheinischen Friedrich-Wilhelms-Universität  
Bonn

March 2019

I hereby declare that this thesis was formulated by myself and that no sources or tools other than those cited were used.

Bonn, .....  
Date

.....  
Signature

1. Gutachter: Prof. Dr. Dieter Meschede
2. Gutachter: Prof. Dr. Simon Stellmer

# Acknowledgements

---

First of all, I have to thank Prof. Dr. Meschede for offering me this fascinating master thesis topic in his research group and Prof. Dr. Simon Stellmer for being the second referee.

Furthermore, I would like to thank Dr. Wolfgang Alt, Dr. Hannes Pfeifer and Dr. Deepak Pandey for helpful ideas and suggestions not only regarding physical, but also technical difficulties as well as their supporting and constructive criticism, which made this master thesis to an instructive and educational experience for me.

Moreover, I have to mention the support of the complete FCQED team including Dr. Jose Gallego, Eduardo Urunuela, Tobias Macha, Carlos Saavedra and Pooja Malik for discussions during group meetings and their help getting me started in the lab.

Also, I want to thank the whole group for sharing knowledge and experience. In special I want to mention Richard Winkelmann, who helped me, although he is working on another experiment.

Additionally I want to thank my office neighbors Lukas Ahlheit, Maximilian Ammenwerth and Dr. Muhammad Sajid for discussing problems and trying to help me in various situations.

Special thanks also go to the proof readers of this thesis, Dr. Hannes Pfeifer, Dr. Deepak Pandey and Lukas Ahlheit.



# Contents

---

<b>1</b>	<b>Introduction</b>	<b>1</b>
<b>2</b>	<b>Theoretical Background on Fiber Fabry-Perot Cavities</b>	<b>3</b>
2.1	Optical Fibers . . . . .	3
2.1.1	Step-Index Fibers . . . . .	3
2.1.2	Graded-Index Fibers . . . . .	5
2.2	Fabry-Perot Cavities . . . . .	8
2.2.1	Resonator Stability . . . . .	10
2.2.2	Resonator Modes and Gaussian Beams . . . . .	10
2.2.3	Coupling to a Cavity Mode . . . . .	12
2.2.4	Fiber Fabry-Perot Cavity Line Shape . . . . .	13
<b>3</b>	<b>Fiber Mirror Production</b>	<b>15</b>
3.1	Laser Ablation Process . . . . .	15
3.2	Production Facility . . . . .	16
3.3	Shooting Technique . . . . .	18
3.4	Surface Reconstruction . . . . .	19
3.5	Obtained Structures . . . . .	21
<b>4</b>	<b>Fiber Fabry-Perot Cavity Assembly</b>	<b>23</b>
4.1	Optical Setup for Cavity Lineshape Observation . . . . .	23
4.2	Observing the Cavity Resonance . . . . .	24
4.2.1	Cavity Line Shape from Reflection Measurement . . . . .	24
4.2.2	Obtained Finesse . . . . .	25
4.3	Cavity Assembly Steps . . . . .	25
4.4	Vacuum System . . . . .	28
4.5	Annealing Process . . . . .	29
<b>5</b>	<b>Enhancing the Mode-Matching of Fiber Fabry-Perot Cavities</b>	<b>31</b>
5.1	Choice of Fiber . . . . .	31
5.2	Fiber Cleaving . . . . .	32
5.2.1	Cleave Tension . . . . .	32
5.2.2	Cleave Length Control . . . . .	34
5.3	Fusion Splicing . . . . .	34
5.3.1	Splice Procedure . . . . .	36
5.3.2	Optimizing Splice Settings . . . . .	36
5.4	Exiting Mode Characterization . . . . .	37
<b>6</b>	<b>Conclusion and Outlook</b>	<b>43</b>

<b>Bibliography</b>	<b>45</b>
<b>A Useful information</b>	<b>49</b>
A.1 Optimized Splice Parameters . . . . .	49
<b>List of Figures</b>	<b>51</b>

---

## Introduction

---

In 1946, E. M. Purcell *et al* measured a decay time reduction of a nuclear spin excitation from the expected "several hours" to less than one minute after coupling a paraffin solid to a resonant cavity [1]. This was one of the first experiments proving that the process of spontaneous emission is influenced by surroundings.

Fermi's Golden Rule shows that the decay rate of an excited atom is proportional to the density of final states. For transitions between discrete levels in atoms, the density of states equals the density of photon states [2]. Nowadays, suitable electromagnetic environments can be designed and produced according to the specific application. If atoms are placed inside a cavity, where for example the mirror distance is less than half the emission wavelength, the excited state lifetime is enlarged [3]. Provided a coupling to a resonant cavity, the density of states is raised causing the enhancement of spontaneous emission, called Purcell effect. A strong Purcell effect in an atom-fiber cavity system has also been reported by our research group [4].

By the coupling to cavities, it is possible to improve the light-matter interaction to the single photon and single emitter level [5]. The interaction between the resonant intra-cavity field and the atom is characterized by three numbers, namely the coupling rate  $g$ , the free-space decay rate of the excited atom  $\gamma$  and the loss rate  $\kappa$ , by which photons leave the cavity through the mirrors [2]. The coupling rate is proportional to the dipole moment  $\mathbf{d} \cdot \mathbf{E} \propto V^{-1/2}$  with the mode volume  $V$ .

Fiber Fabry-Perot cavities provide the significant advantage of miniaturized mode volume, as the mirror distance can be in the order of a few  $10\ \mu\text{m}$ . The waist sizes of Gaussian modes are usually much lower than  $10\ \mu\text{m}$ . Because of this small size, the high coupling regime ( $g \gg \kappa, \gamma$ ) can be achieved for a variety of emitters, even in case of a broadband cavity with large  $\kappa$ . This includes neutral atoms [6], ions [5], nitrogen-vacancy centers [7], Bose-Einstein condensates [8, 9] and solid-state emitters like quantum dots [10].

Despite the small mode volume, fiber cavities can provide direct optical access to the cavity mode. Depending on the cavity design, even mechanical objects can be introduced into the cavity volume allowing the usage of optomechanics inside the resonator volume [11].

Other advantages are the directly fiber coupled in- and output channels. The fiber coupling and the compact overall size make fiber cavities compatible with atom chips [12, 13].

However, low spacial mode-matching between the fiber and the cavity mode leads to an inefficient coupling of light from the fiber into the cavity and vice versa. Thus, a photon retrieved from an emitter inside the resonator has a higher probability of being lost, since it is not guided in the fiber. Especially for processes with single photons as e.g. in quantum information applications, a high mode-matching is indispensable.

A fully fiber integrated way to enhance the mode-matching is to apply optics in the form of graded-index fiber lenses, as it is presented by G.K. Gulati *et al* [14]. To determine the cavity length, a multimode fiber piece of a specific size is used to terminate the assembly and act as a substrate for the fiber mirror. This concept requires precise control over the length of the fiber pieces and advanced splicing techniques with low losses and negligible mode deterioration. In their work, all used fibers with different outer diameters complicating the handling of the fiber mirrors. In this thesis, it has been tried to produce an assembly of equally sized fibers with 125  $\mu\text{m}$  diameter. Further, elaborate ways of length control and fiber splicing have been investigated, enhancing the quality of fiber lens based mode-matching optics.

Based on the specific application, one requires fiber mirrors of different radii of curvature and diameter. To implement state-of-the-art fiber mirror production techniques in our research group, a new versatile laser ablation setup has been built. This allows the production of ultra-smooth mirror surfaces with much larger range of radii of curvature and diameters compared to the old one.

Further, a new assembly setup for fiber cavities has been realized. This setup is used for fabricating and characterizing cavities for the FCQED experiment of this research group.

With the given advantages, fiber Fabry-Perot cavities are used in numerous applications, e.g. in our photon storage and retrieval experiment or in quantum repeater nodes [15]. By efficiently interfacing almost any emitter, they are also expected to improve the performance of single-photon sources and quantum memories [8, 16]. Apart from quantum information, numerous possible fields of application can be listed, e.g. spectral filtering of light or cavity enhanced spectroscopy [17].

In the following chapter, theoretical fundamentals of fiber Fabry-Perot cavities will be presented.

To give a full picture of the fabrication process of mode-matched optical fiber cavities the procedure of fabricating mirror surfaces is described in chapter 3. There, the principle of laser ablation and the production setup is explained. Further, a surface reconstruction method and obtained cross-sections of a processed fiber are shown.

Chapter 4 deals with the assembly of cavities for our experiment from the retrieved fiber mirrors. Here, the cavity design and its specific production procedure are introduced. It is followed by a description of the technique to retrieve information about the coupling and the finesse by resonance observation.

In the last chapter, the procedures to enhance the spatial mode-matching between fiber and cavity mode are presented.

---

# Theoretical Background on Fiber Fabry-Perot Cavities

---

Fabry-Perot cavities are resonators for light, within high field amplitudes and tight spatial confinement can be achieved. By placing e.g. an atom inside a resonant cavity, the interaction probability between photon and atom can be enhanced, which is described by the field of cavity quantum electrodynamics (CQED) [2]. This principle is widely used not only in quantum information experiments as ours [18], but also plays an important role for spectroscopy and sensing [17, 19].

A particular example of miniaturized cavities is fiber Fabry-Perot cavities that are built by micromachining the mirrors directly onto fiber end facets. For understanding the different production and alignment steps, a general overview of fibers, cavities, resonator modes and the coupling to cavity modes is provided.

## 2.1 Optical Fibers

Optical fibers are thin and flexible dielectric waveguides with a circular cross-section, which are produced for guiding light over distances up to several hundred kilometers in telecommunication technology. Information encoded in photons can travel in such waveguides with low losses and negligible decoherence. This makes fibers a useful tool for transmitting quantum information [20].

The most common material for fiber production is fused silica,  $\text{SiO}_2$ , which provides high mechanical stability against pulling forces. As the refractive index in the central region is increased by dopants (e.g. germanium dioxide) compared to the surrounding cladding, total internal reflection allows to guide light in the this so-called core. The guiding properties are determined by the number of cores, their diameter and the refractive index profile [21]. To give an overview of the optical fibers that are relevant for this thesis, two kinds of single core fibers are discussed here: step-index and graded-index (GRIN) fibers.

### 2.1.1 Step-Index Fibers

As it is illustrated in figure 2.1, step-index fibers are characterized by a constant core and cladding index and a sharp transition from core to cladding. One important figure describing their modal properties is the V-parameter, which is defined as

$$V = \frac{\omega a}{c} \cdot NA, \quad (2.1)$$

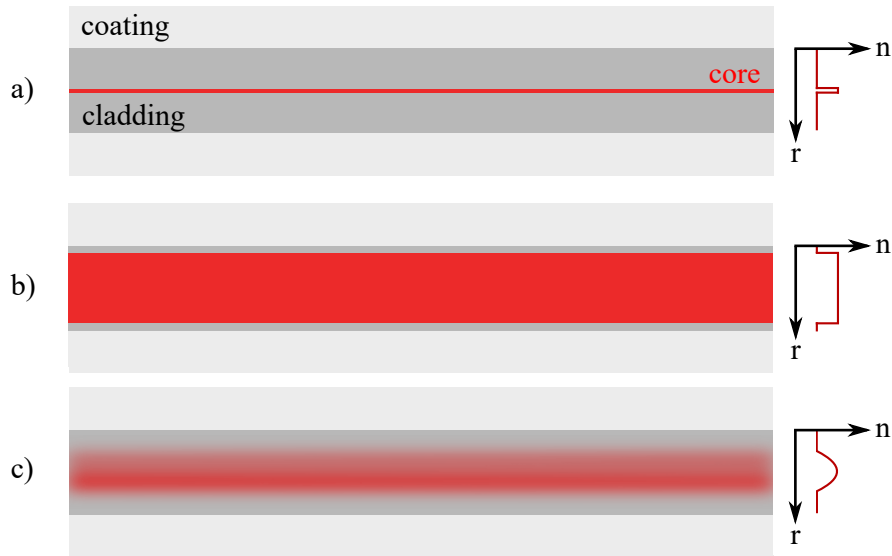


Figure 2.1: This sketch illustrates the structure of fibers with their refractive index profile. The light is guided in the core, which is surrounded by the cladding to create a refractive index transition. Around the fiber, a coating is applied for protection.

where  $\omega$  denotes the angular frequency of the light,  $a$  the core radius,  $NA$  the numerical aperture and  $c$  the speed of light.

For  $V < 2.405$ , the fiber is called a single-mode fiber, because only the fundamental Gaussian mode is guided. The wavefronts in a single-mode fiber are plane and perpendicular to the propagation direction. When the light is coupled out, it leaves the fiber as a Gaussian beam with a waist of the mode field diameter in the fiber [21].

For  $V \gg 1$ , the number of guided modes scales quadratically with  $V$  [21]. A ray tracing picture of modes in single- and multi-mode fibers is shown in figure 2.2 a) and b).

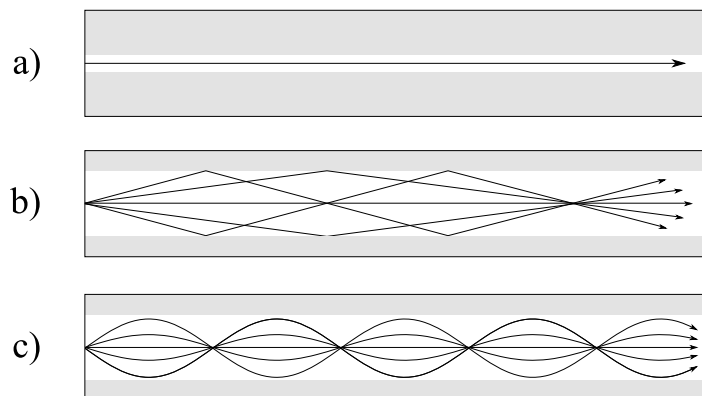


Figure 2.2: This figure shows ray tracing pictures of modes in a): single-mode fibers, b) multi-mode fibers and c): graded-index fibers. The image is taken from [22].

### 2.1.2 Graded-Index Fibers

Graded-index (GRIN) fibers are doped such that the refractive index profile can be in first order approximated by

$$\begin{aligned} n(r < a) &= n_1 \cdot \left(1 - \Delta \left(\frac{r}{a}\right)^2\right) \\ n(r \geq a) &= n_2, \end{aligned} \quad (2.2)$$

where  $r$  denotes the radial coordinate and  $a$  the core radius. In this equation  $\Delta = (n_1 - n_2)/n_1$  holds true. The index decreases quadratically from the central core index  $n_1$ , until it reaches the cladding index  $n_2$  (see figure 2.1) [23]. In this approach and assuming paraxial approximation, light rays perform radial oscillations with the amplitude  $r_0$ , when propagating in  $z$ -direction:

$$r(z) = r_0 \cdot \sin(2\pi z/\Lambda) \quad \text{with the period} \quad \Lambda = \frac{2\pi a}{\sqrt{2\Delta}}, \quad (2.3)$$

as depicted in figure 2.2 c).

For a GRIN-fiber sample an ABCD-matrix can be set with wave number constant  $K = 2\pi/\Lambda$  and length  $l$ :

$$M(l) = \begin{pmatrix} \cos(Kl) & K^{-1} \sin(Kl) \\ -K \sin(Kl) & \cos(Kl) \end{pmatrix}. \quad (2.4)$$

Consequently, a short piece of GRIN fiber that fulfills the condition  $Kl < \pi/4$ , acts as a lens [23] and can be spliced to a fiber probe to optimize its output beam. These so-called fiber lenses have the advantage that they are automatically aligned and the position is fixed due to a mechanically stable connection. They are used in different fields such as optical coherence tomography for medical applications [24], enhancing coupling efficiencies into fibers with different mode field diameter [25] or in fiber cavity assemblies [14]. Since mode distortions as introduced by e.g. aberrations can lead to decreased coupling efficiencies or obstructed images, it is very important to characterize the properties of these lens systems in detail. The subsequent section follows reference [26].

### Optical Aberrations of GRIN Fiber Lenses

Measurements of the index profile in GRIN fibers often reveal deviations from the quadratic shape. Especially fibers produced with old fabrication techniques exhibit Gaussian dips in the core index profile. Modern high bandwidth GRIN fibers are often optimized for minimal intermodal pulse broadening in the operating wavelength regime by adapting the exponent of  $(r/a)$ , in the following called  $\alpha$ . Furthermore, ripples can occur due to imperfections of the fabrication process.

A more complex model that is able to account for a deviation in  $\alpha$ , a central Gaussian dip with width  $w_{\text{dip}}$  and sinusoidal ripple was introduced by [26]:

$$n(r) = \begin{cases} n_1 \left[ 1 - 2\Delta \left( \left(\frac{r}{a}\right)^\alpha + h_{\text{dip}} e^{-\left(\frac{r}{w_{\text{dip}}}\right)^2} \right) \right] + h_{\text{rip}} \Delta n \sin(2\pi r/p_{\text{rip}}), & \text{if } r < a \\ n_1 (1 - 2\Delta)^{1/2}, & \text{if } r \geq a. \end{cases} \quad (2.5)$$

Hereby,  $\Delta n = n_1 - n_2$  and  $\Delta = (n_1^2 - n_2^2)/(2n_1^2) \approx (n_1 - n_2)/n_1$  holds true for a small  $\Delta n$ .  $h_{\text{dip}}$  and  $w_{\text{dip}}$  denote the amplitude and the width of the dip,  $h_{\text{rip}}$  and  $p_{\text{rip}}$  the amplitude and the periodic length of the ripple.

Based on this model, Lorensen *et al* have shown numerical predictions of the beam propagation to investigate the aberrations caused by these index profile deviations [26]. These predictions agree with measurements, which are shown below. Within their work, they use a combination of a single-mode fiber with a mode field diameter of  $5 \mu\text{m}$  and a  $275 \mu\text{m}$  long section of no-core fiber for beam expansion. From there, the beam is launched into a GRIN fiber with  $a = 100 \mu\text{m}$ ,  $\Delta = 2\%$  and  $n_2 = 1.453$ . One figure of merit to characterize aberrations is the Strehl ratio, which is defined as the ratio of the focal spot intensity of an aberrated system to that of a diffraction-limited one. In the following, results from Lorensen *et al* are summarized [26]:

### The Effect of the Power Law Exponent

To evaluate the effect of the power law exponent, simulations with different coefficients  $\alpha$  have been performed. Here, the central index dip and the ripple is neglected. A discrepancy in  $\alpha$  leads to spherical aberrations, whereas  $\alpha > 2$  creates positive and  $\alpha < 2$  negative spherical aberrations respectively. Additionally, the detuning modifies the paraxial focussing power of the lens, which changes the focal length in reversed direction compared to the focus shift caused by the spherical aberration.

In case of  $\alpha = 2.15$ , the Strehl ratio  $S$  takes the value 0.77. For  $\alpha = 1.85$ ,  $S$  equals 0.96.

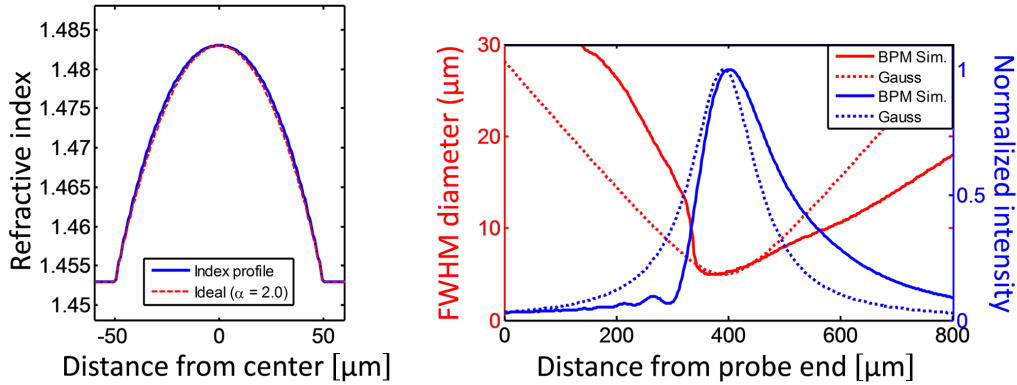


Figure 2.3: On the left-hand side, the refractive index profile of a GRIN fiber with  $\alpha = 2.15$  is shown (blue) with a comparison to a profile with  $\alpha = 2$  is shown. On the right, the beam widths and normalized on-axis intensities are given as a subject to the distance from the probe end. They reveal the typical behavior for a beam passing a lens with strong positive spherical aberration. The figure is taken from [26].

### The Effect of a Central Refractive Index Dip

The index dip in the core center has a similar impact as a lens with negative focal length, which is spatially restricted to the very inner part of the core. The light is diffracted with an angle, which can be large enough so that it cannot be refocussed by the fiber. The light in the outer part is considered to experience an aberration-free refocussing. Both "light beams" interfere with each other leading to a mode propagation, which can be seen in figure 2.6. It is striking that the mode has a donut shape in the region directly adjacent to the GRIN fiber.

The width  $w_{\text{dip}}$  is the most critical parameter, because it determines the fraction of the deflected power. With  $w_{\text{dip}} = 1.5 \mu\text{m}$  and  $h_{\text{dip}} = 0.5$  the Strehl ratio is calculated to be 0.97. Doubling the width lowers it to 0.88, whereas doubling the depth  $h_{\text{dip}}$  leads to a Strehl ratio of 0.96.

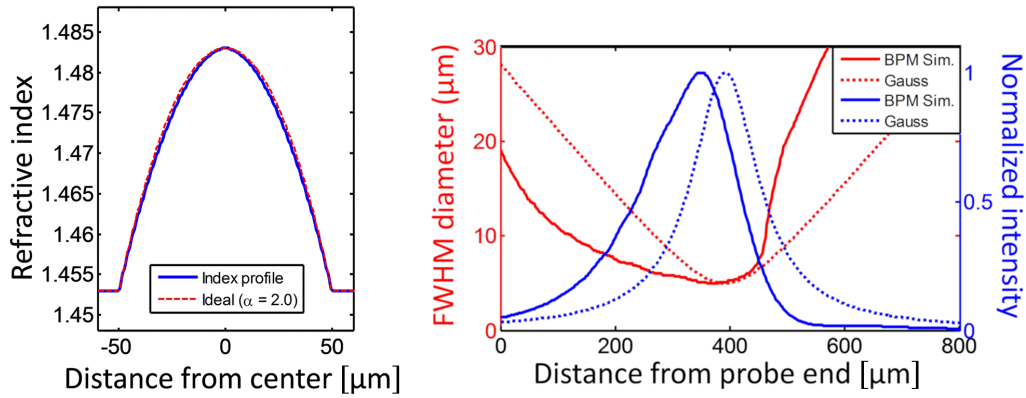


Figure 2.4: Here, similar to figure 2.4 an index profile of a GRIN fiber is displayed with  $\alpha = 1.85$ . Additionally, the beam widths as well as the normalized on-axis intensities are shown with respect to the fiber probe distance. As an exponent of  $\alpha = 2.15$  shows positive spherical aberrations, this one shows a strong negative one. This picture is taken from [26].

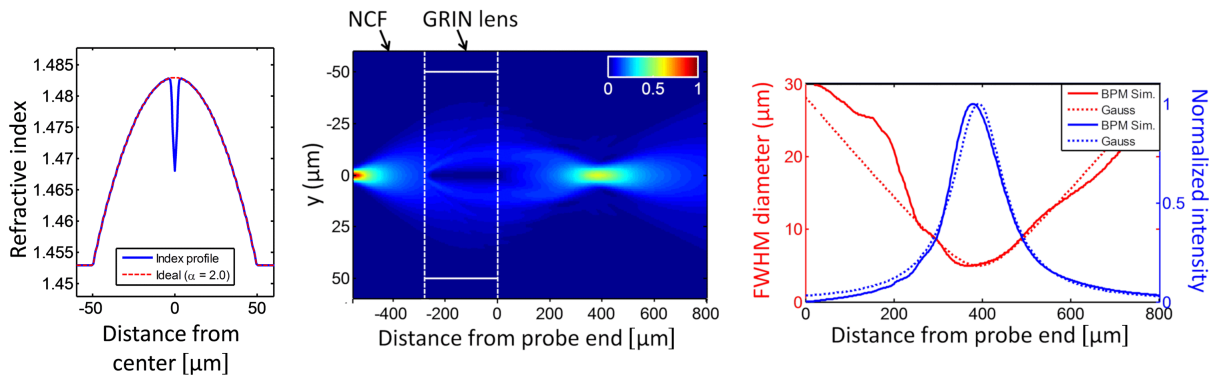


Figure 2.5: On the left, a refractive index profile is presented with  $\alpha = 2$  and a central dip of width  $w_{\text{dip}} = 1.5 \mu\text{m}$   $h_{\text{dip}} = 0.5$ . The central figure shows the spatial light intensity distribution illustrating the donut shape of the mode inside the GRIN fiber. The beam diameter at different distance from the fiber tip and the normalized on-axis intensities are displayed on the right. The image is taken from [26].

### The Effect of the Index Ripple

The influence of the index ripple in a piece of GRIN fiber can be compared to the one of a phase grating. Nevertheless, the in reality occurring ripple amplitudes are too low to have a significant impact on the Strehl ratio. However, predictions of the beam propagation in the near-field of the GRIN fiber are more precise, if a ripple with a periodic length of  $p_{\text{rip}} \approx a/3$  and amplitudes  $h_{\text{rip}} \approx 0.01$  is added.

After this introduction into fibers, the following section deals with the theoretical principles of optical cavities.

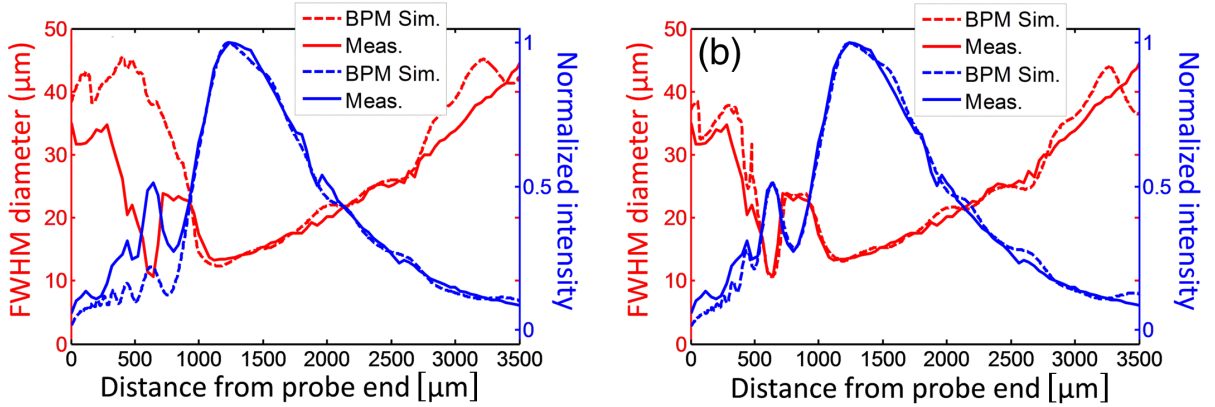


Figure 2.6: Prediction and measurement of the beam propagation after a fiber lens from 100/140 MMF POFC GRIN fiber. The prediction without a long ripple is displayed on the left, the one with it is on the right. The image is taken from [26].

## 2.2 Fabry-Perot Cavities

In a simple form, cavities consist of two opposite planar mirrors with ideal reflectivity, which reflect the light such that it forms a standing wave. To accomplish high field strength, a light wave must reproduce itself after one roundtrip so that the gained phase after this way is  $2\pi$ . This condition leads to  $l = m \cdot \lambda / (2n)$  with the length of the cavity  $l$ , the number of intensity maxima  $m$ , the wavelength of the light  $\lambda$  and the refractive index of the material between the mirrors  $n$ .

This condition is fulfilled for multiple wavelengths, forming longitudinal modes. They are spectrally separated from each other by one free-spectral range, given by [27]

$$\Delta\nu_{FSR} = \frac{c}{2nl}. \quad (2.6)$$

For ideal mirrors, the linewidth of the cavity resonances  $\Delta\nu$  is infinitesimally small.

In reality, mirrors have reflection coefficients of  $R_i = |r_i|^2 < 1$  with  $i \in \{1, 2\}$ . In this case and assuming a constant incoupled electric field, the cavity transmission spectrum (as it is shown in figure 2.7) is given by

$$P_{\text{trans}} = P_{\text{in}} \cdot \frac{1}{1 + \left(\frac{2\mathcal{F}}{\pi}\right)^2 \sin^2(\Phi/2)} \quad \text{with} \quad \Phi = \frac{4\pi nl}{\lambda}, \quad (2.7)$$

where  $\Phi$  is the round-trip phase shift and  $\mathcal{F}$  finesse [2]. As it is illustrated in this figure, the finesse can be defined as  $\mathcal{F} = 2\pi/\Delta\Phi$  with the full-width at half maximum  $\Delta\Phi$ . Since the phase behaves proportional to the frequency, it also describes the ratio of the free-spectral range to the linewidth of one cavity resonance. It can be shown that in a lossless cavity the finesse only depends on the mirror reflectivities [2]:

$$\mathcal{F} = \frac{\Delta\nu_{FSR}}{\Delta\nu} = \frac{\pi(r_1 r_2)^{1/2}}{1 - r_1 r_2}. \quad (2.8)$$

To account for absorption losses during one roundtrip, the factor  $r_1 r_2$  in equation 2.8 can be replaced by the exponential factor  $r^2 = r_1 r_2 \exp(-2\alpha_s d)$ , where  $\alpha$  denotes the absorption coefficient of the gas in the cavity [28]. Also each mirror introduces the following loss sources, which are expressed in terms

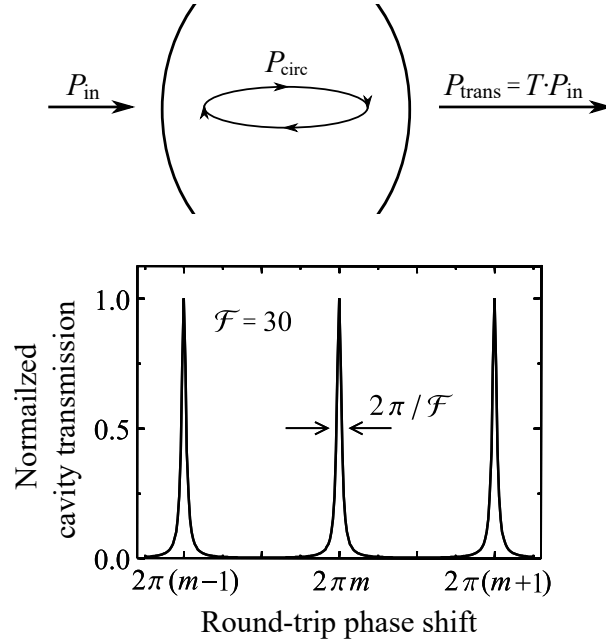


Figure 2.7: This figure illustrates the definition of the incoming power  $P_{\text{in}}$ , from which a part is coupled into the cavity. The power circulating in the cavity is called  $P_{\text{circ}}$  and the transmitted one  $P_{\text{trans}}$ , which is spectrally depicted in the lower part. Parts of this figure are taken from [2].

of intensity decrease: absorption occurring in the mirror coatings  $\mathcal{L}_{\text{abs}}$ , scattering due to mirror surface roughness  $\mathcal{L}_{\text{scatt}}$ , the finite mirror transmission coefficients  $T$  as well as beam clipping on the mirrors  $\mathcal{L}_{\text{clip}}$ . This influences the finesse according to [29]

$$\mathcal{F} = \frac{2\pi}{\sum_{i=1,2} (\mathcal{L}_{\text{abs},i} + \mathcal{L}_{\text{scatt},i} + \mathcal{L}_{\text{clip},i} + T_i)}, \quad (2.9)$$

where the clipping loss for each mirror  $i = 1, 2$  and a Gaussian mode can be calculated by using

$$\mathcal{L}_{\text{clip},i} = \exp\left(2 \frac{(D_i/2)^2}{w_i^2}\right) \quad (2.10)$$

with the diameter of mirror  $i$ ,  $D_i$ , and the mode radius on the respective mirror,  $w_i$ . Hence, losses decrease the finesse and broaden the linewidth  $\Delta\nu$ .

For high finesse cavities ( $R_1 = R_2 \approx 1$  and negligible losses), the cavity loss rate  $\kappa$  can be directly determined from the cavity parameters and equals the spectral cavity linewidth [2]

$$\kappa = \frac{c(1-R)}{nl}. \quad (2.11)$$

This quantity describes the photon number decay by  $N(t) = N(0) \exp(-\kappa t)$ , if no photons are coupled into the resonator. Due to this exponential decay in time domain, the spectral line shape for each mode

becomes a Lorentzian function

$$\gamma(\nu) = \frac{\kappa^2}{\kappa^2 + 4(\nu - \nu_0)^2}, \quad (2.12)$$

with  $\nu$  the frequency of the light and  $\nu_0$  the cavity resonance frequency [2].

### 2.2.1 Resonator Stability

So far, it has been neglected that most cavities do not have plane mirrors. In general, different mirror geometries are possible for a stable operation, as long as they fulfil the stability criterion

$$0 \leq g_1 g_2 \leq 1 \quad \text{with} \quad g_{1,2} = 1 - l/\rho_{1,2}, \quad (2.13)$$

where  $\rho_{1,2}$  denotes the radius of curvature of mirrors 1 and 2 respectively<sup>1</sup> and  $l$  the mirror distance [23]. For building cavities, it is convenient to go for concentric cavities with  $\rho_1 = \rho_2 = l/2$ , since their stability is not as fragile with respect to alignment imperfections compared to confocal ones<sup>2</sup> [6].

The cavity geometry also determines the shape of the light modes inside the resonator, which is described in the following section.

### 2.2.2 Resonator Modes and Gaussian Beams

The electric field distribution of cavity modes is such that they have to reproduce themselves after two reflections. This condition allows the existence of higher-order transversal modes, so-called TEM<sub>nm</sub> modes. They can occur, if they are solutions of the paraxial Helmholtz equation with the boundary condition that the wavefronts match the mirror curvatures. Depending on the cavity design, the frequency degeneracy is lifted, so that they appear separately in a cavity spectrum [30]. For a sketched cavity spectrum and the intensity pattern of the TEM<sub>nm</sub>, see figure 2.8.

The fundamental mode, also called TEM<sub>00</sub> mode, is the most desirable one for our purposes, because it is equivalent to a Gaussian beam with an axial field distribution of

$$E(r, z) = E_0 \frac{w_0}{w(z)} \exp\left(\frac{-r^2}{w(z)^2}\right) \exp\left(-i\left[kz + k\frac{r^2}{2R(z)}\right]\right) \exp(i\zeta(z)), \quad (2.14)$$

where the following parameters are defined as

$$\text{the beam radius} \quad w(z) = w_0 \sqrt{1 + \left(\frac{z}{z_0}\right)^2}, \quad (2.15)$$

$$\text{the wavefront radius of curvature} \quad R(z) = z \left(1 + \left(\frac{z_0}{z}\right)^2\right), \quad (2.16)$$

$$\text{the Gouy-phase} \quad \zeta(z) = \tan^{-1}\left(\frac{z}{z_0}\right) \quad (2.17)$$

$$\text{and the Rayleigh range} \quad z_R = \frac{\pi w_0^2}{\lambda}. \quad (2.18)$$

<sup>1</sup>  $\rho < 0$  for concave and  $\rho > 0$  for convex structures

<sup>2</sup> confocal cavity:  $\rho_1 = \rho_2 = l$

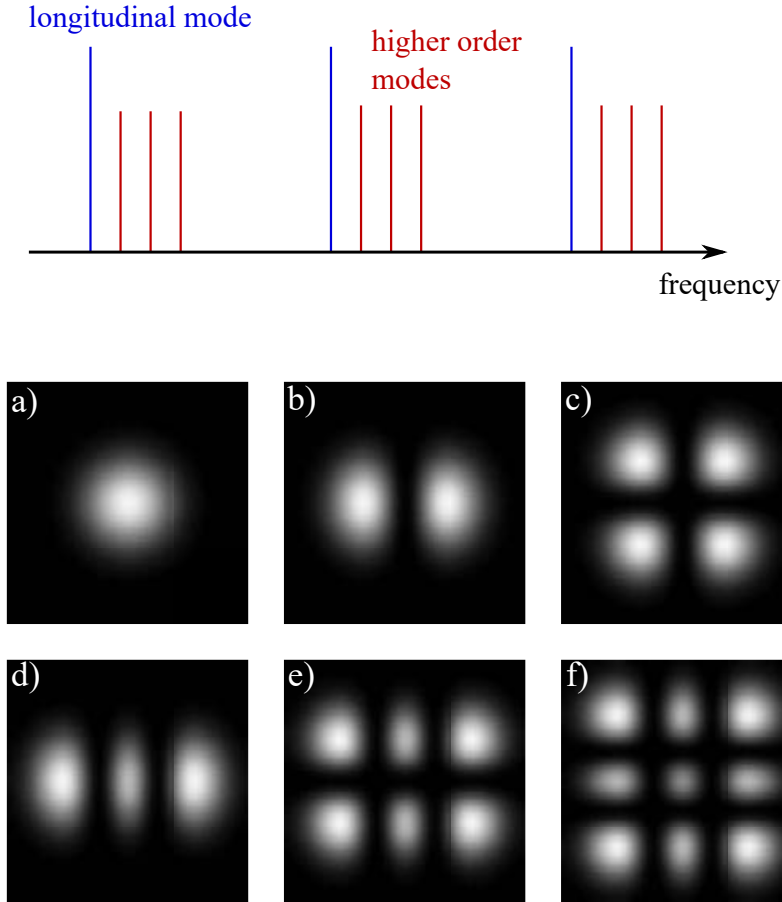


Figure 2.8: The upper part shows a cavity spectrum with longitudinal and higher order transversal ( $TEM_{nm}$ ) modes. In the lower one intensity distributions of higher order transversal modes are presented:

- a):  $TEM_{00}$  mode      b):  $TEM_{10}$  mode      c):  $TEM_{11}$  mode  
d):  $TEM_{20}$  mode      e):  $TEM_{21}$  mode      f):  $TEM_{22}$  mode.

Thereby the numbers  $n$  and  $m$  give number of intensity minima with respect to the horizontal and vertical axis.

The coordinate  $z$  denotes the distance to the waist position, where the beam has its minimal radius of  $w_0$ . For  $r = w(z)$  the intensity  $I \propto |E(r, z)|^2$  decreased to  $1/e^2$  of its on-axis value. A sketch of a Gaussian mode in a cavity is depicted in figure 2.9.

For elliptic mirrors the paraxial resonator theory treating modes as scalar functions has to be modified to a vector theory, which leads in first order to a polarization dependent frequency splitting of resonator modes. A correction term accounts for the deviation from the paraxial theory. It depends only on the radii of curvature, along which the mode is polarized. For the case of a plano-concave cavity and the wave polarized along the principal axes with radii of curvature  $\rho_{1,2}$ , Uphoff *et al* calculated the splitting to be

$$\delta\nu = \frac{\Delta\nu_{FSR}}{2\pi k} \cdot \frac{\rho_1 - \rho_2}{\rho_1\rho_2}. \quad (2.19)$$

For reducing the splitting, the mirrors can be rotated around the cavity axis. The minimal splitting is achieved, when the major axes of the mirrors are perpendicular to each other [31].

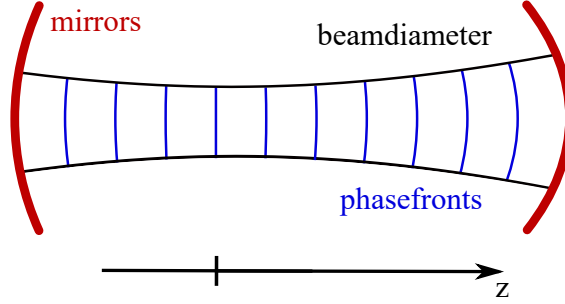


Figure 2.9: Fundamental Gaussian mode in a cavity.

### 2.2.3 Coupling to a Cavity Mode

In the following sections, a compact notation for light fields is used to keep equations short. An electric field is expressed as  $E_i = \mathcal{E}_i |\psi_i\rangle$  with its complex amplitude  $\mathcal{E}_i$  containing the time dependency  $\exp(-i\omega t)$ . The spatial mode components  $|\psi_i\rangle$  are given in Dirac notation. All modes  $|\psi_i\rangle$  are normalized such that  $\langle \psi_i | \psi_i \rangle = 1$  holds true [32]. Forward propagating modes (from left to right in figure 2.11) are marked with the superscript +, backward propagating modes with a minus sign, respectively.

To couple light efficiently into the the cavity mode  $|\psi_{\text{cav}}\rangle$ , the mode of the incoming light  $|\psi_{\text{in}}\rangle$  has coincide with  $|\psi_{\text{cav}}\rangle$ . A figure of merit for their spacial overlap is the mode-matching efficiency  $\epsilon_1$  at the incoupling mirror defined by

$$\epsilon_1 = |\langle \psi_{\text{in}}^+ | \psi_{\text{cav}}^+ \rangle|^2 = \left| \int (\psi_{\text{in}}^+)^* \psi_{\text{cav}}^+ dA \right|^2. \quad (2.20)$$

While the mode-matching in free-space coupled cavities can always be adjusted by positioning the beam and converting the laser mode with lenses, the coupling to a fiber Fabry-Perot cavity cannot be altered once the mirrors are fixed with respect to each other. In a simple model, assuming Gaussian modes, the mode overlap can be expressed as [32]

$$\epsilon_c = \frac{4}{\left( \frac{w_f}{w_{\text{cav}}} + \frac{w_{\text{cav}}}{w_f} \right)^2 + \frac{s^2}{z_{\text{R},f} z_{\text{R},\text{cav}}}}, \quad (2.21)$$

where  $w_f$  and  $w_{\text{cav}}$  are the waist sizes of the fiber- and the cavity mode,  $z_{\text{R},f}$  and  $z_{\text{R},\text{cav}}$  their Rayleigh ranges and  $s$  the distance of their waist positions.

An additional angle  $\theta$  between mirror surface normal and fiber core and a decentration  $d$  between mirror and fiber core (see figure 2.10) leads to an exponential decrease of the mode-matching such that  $\epsilon_1$  is written as [33]

$$\epsilon_1 = \epsilon_c \cdot \exp \left[ - \left( \frac{d}{d_0} \right)^2 - \left( \frac{\theta}{\theta_0} \right)^2 \right], \quad (2.22)$$

with the angle and decentration tolerances  $\theta_0$  and  $d_0$ . Further description and expressions to calculate these values can be found in reference [32].

Equation 2.21 shows that the mode-matching reduces drastically for long symmetric cavities made of single-mode fibers. In this case, there is a strong discrepancy of  $w_{\text{cav}}$  and  $w_f$  because of the diverging nature of cavity modes and the small core size of single-mode fibers. Additionally,  $s = l/2$  becomes large, whereas the optimal overlap is given for  $w_f = w_{\text{cav}}$  and  $s = 0$ .

The mode-matching can be obtained from the line shape of the reflected power by the cavity, which is further discussed in the following section.

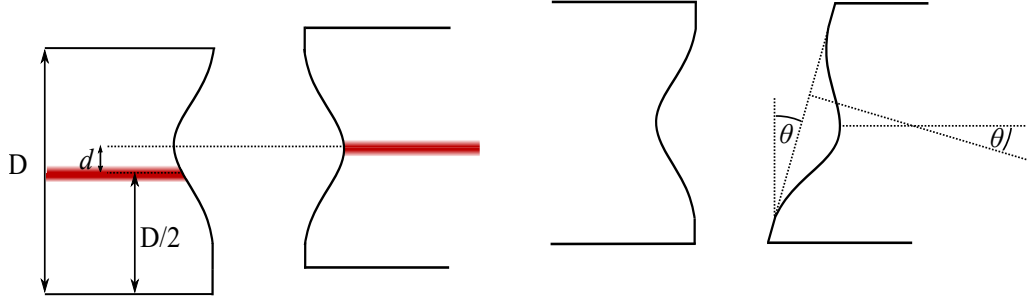


Figure 2.10: This figure illustrates the definition of decentrations of mirror and core (marked in red)  $d$ , as well as angles of the mirror with respect to the fiber axis normal  $\theta$ .

### 2.2.4 Fiber Fabry-Perot Cavity Line Shape

The theory part below follows reference [18] by J. Gallego *et al.* For traditional cavities the recorded power in reflection direction is a Lorentzian dip with respect to  $\delta\nu = 2\pi(\nu_{\text{laser}} - \nu_{\text{cav}})/\kappa$

$$\frac{P_{\text{out}}}{P_{\text{in}}} = 1 - \eta_{\text{dip}} \frac{1}{1 + \delta\nu^2} \quad \text{with} \quad \eta_{\text{dip}} = \epsilon_1 \left( 1 - \frac{(\mathcal{T}_1 - \mathcal{T}_2 - \mathcal{L}_1 - \mathcal{L}_2)^2}{(\mathcal{T}_1 + \mathcal{T}_2 + \mathcal{L}_1 + \mathcal{L}_2)^2} \right), \quad (2.23)$$

where  $\mathcal{T}_i$  and  $\mathcal{L}_i$  denote power transmission and losses of the  $i$ -th mirror respectively.

The main difference between fiber Fabry-Perot and traditional cavities are the directly fiber coupled in- and output channels. In the case that the fiber mode and the cavity mode are not matching, the field propagating in reflection direction  $E_{\text{out}}$  is mode filtered, which leads to a change of the line shape. It is built up by the interference of two fields (see figure 2.11): One arises from the incoming light, that is directly reflected at the incoupling mirror and hence does not enter the cavity. In the following it is called  $E_r$ . The other one,  $E_{\text{leak}}$ , originates in the leakage field out of the cavity. These fields can be described as

$$E_r = r_1 \mathcal{E}_{\text{in}} |\psi_r\rangle \approx \mathcal{E}_{\text{in}} |\psi_r\rangle \quad (2.24)$$

$$E_{\text{leak}}(\delta\nu) = -\mathcal{E}_{\text{in}} \frac{t_1^2 r_2 \exp(i\Phi)}{1 - r_1 r_2 \exp(i\Phi)} \langle \psi_{\text{cav}}^+ | \psi_f^+ \rangle \langle \psi_{\text{cav}}^- | \psi_f^- \rangle, \quad (2.25)$$

where  $r_i$  and  $t_i$  denote the complex reflection and transmission coefficients,  $\Phi$  the round trip phase,  $\mathcal{E}_{\text{in}}$  the amplitude of the field impinging on the incoupling mirror and  $|\psi_f\rangle$  the fiber mode.

With this,  $E_{\text{out}}$  can be expressed as

$$E_{\text{out}} = \mathcal{E}_{\text{in}} \left( \langle \psi_f^- | \psi_r \rangle + \frac{t_1^2 r_2 \exp(i\Phi)}{1 - r_1 r_2 \exp(i\Phi)} \langle \psi_{\text{cav}}^+ | \psi_f^+ \rangle \langle \psi_f^- | \psi_{\text{cav}}^- \rangle \right) |\psi_f^- \rangle \quad (2.26)$$

and the power  $P_{\text{out}}$  is approximated for  $\delta\nu/\Delta\nu_{\text{FSR}} \ll 1$

$$\frac{P_{\text{out}}(\delta\nu)}{P_{\text{in}}} = \eta_r - \eta_{\mathcal{L}} \left( \frac{1}{1 + \delta\nu^2} - \mathcal{A} \frac{\delta\nu}{1 + \delta\nu^2} \right), \quad (2.27)$$

where  $\eta_{\mathcal{L}}$  describes the Lorentzian and  $\mathcal{A}$  the relative amplitude of the asymmetric dispersive term. Both  $\mathcal{A}$  and  $\eta_{\mathcal{L}}$  depend on the overlap integrals of  $|\psi_r\rangle$ ,  $|\psi_f\rangle$  and  $|\psi_{\text{cav}}\rangle$ .  $\eta_r$  denotes reflected power proportion due to the mirror reflectivity (further expressions to calculate their values can be found in [18]).

The line shape of the transmitted power  $P_T$  remains a Lorentzian, since only the leakage field of the cavity plays a role. Its maximum is given by

$$\frac{P_{T,\text{max}}}{P_{\text{in}}} = \epsilon_1 \epsilon_2 \frac{4\mathcal{T}_1\mathcal{T}_2}{(\mathcal{T}_1 + \mathcal{T}_2 + \mathcal{L}_1 + \mathcal{L}_2)^2}, \quad (2.28)$$

where  $\epsilon_2$  denotes the overlap between cavity and transmission fiber mode. Thus, for determining  $\epsilon_1$  only from the transmission signal,  $\epsilon_2$  has to be well known.

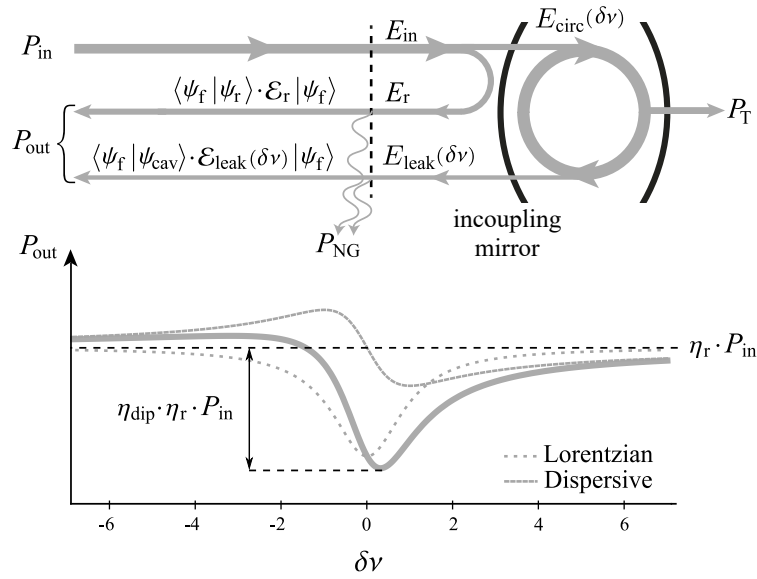


Figure 2.11: This figure illustrates the origin of the asymmetric reflection lineshape of fiber Fabry-Perot cavities. The light power propagating in reflection direction,  $P_{\text{out}}$ , is built up by the interference of  $E_r$  and  $E_{\text{leak}}(\delta\nu)$ , whereas some part of the power  $P_{\text{NG}}$  is not guided by the single-mode fiber. The image is adapted from [18].

---

## Fiber Mirror Production

---

Miniaturization of cavities is of interest not only for cavity quantum electrodynamics experiments but also for spectroscopic applications. Conventional spectrometers for aerospace technologies are based on multipass cells, which provide pathlengths of up to 2 m.

In 2012 the rover "Curiosity" landed on Mars amongst others to measure isotope ratios of hydrogen, carbon and oxygen in CO<sub>2</sub> and H<sub>2</sub>O [34]. Its spectrometer<sup>1</sup> provides a double pass absorption region of 25 cm length [35].

In the future, these spectrometers may be replaced by millimeter long fiber cavities. Already a cavity of  $l = 1$  mm with a finesse of 30 000 provides approximately 7 m optical path length and is by far less spacious.

Because of the divergence of the cavity modes, large mirrors have to be used for this application. Since the fiber mirror production facility, that existed before starting this thesis, was limited to mirror diameters of about 50 μm, a new setup was implemented to enable the production of larger mirrors. This work has been performed together with Pia Fürtjes from the research group of Prof. Dr. Michael Köhl [36].

Similarly to the old system, it uses a laser ablation process to carve spherical craters into the fiber end facets, which will be described in the following section. The retrieved fiber facets are characterized using an established surface reconstruction method, which is discussed subsequently.

### 3.1 Laser Ablation Process

Silica provides a strong absorption band for wavelengths between 9.0 μm and 9.5 μm due to Si-O-Si vibration modes [37]. Because of the resulting opaqueness, CO<sub>2</sub> lasers with a wavelength of 9.3 μm can be used for material processing, e.g. melting and evaporating material from a thin layer on the surface. Here, the absorption is used for reproducibly creating depressions, which later will be used as mirrors for optical cavities.

The ablated craters need to have a spherical surface with low roughness and ellipticity to be suitable as cavity mirrors. These conditions can be met by applying radially symmetric Gaussian beam pulses on the surface to be processed. Theoretically it can be shown that a treatment with Gaussian laser pulses with temporally constant intensity profile  $I(\rho) = I \exp(-2\rho^2/w^2)$  can lead to craters, whose radial depths  $z(\rho)$

---

<sup>1</sup> TLAS: tunable laser absorption spectrometer

are given by [38]

$$z(\rho) = z_0 \exp\left(-\frac{U}{k_B T(0, \tau)} \frac{\rho^2}{2w^2}\right), \quad (3.1)$$

where  $z_0$  is the amplitude,  $U = 3.6 \text{ eV}$  is the latent heat of evaporation per atom and  $k_B$  the Boltzmann constant.  $T(0, \tau)$  describes the temperature in the center ( $\rho = 0$ ) directly after a pulse of duration  $\tau$ . It can be expressed as

$$T(0, \tau) = \frac{A(\lambda)P}{\sqrt{2\pi^3} \cdot w\kappa} \cdot \tan^{-1}\left(\frac{2D}{w^2}\tau\right) \quad (3.2)$$

with  $A(\lambda)$  the absorption coefficient,  $P$  the laser power,  $\kappa$  the thermal conductivity and  $D$  the diffusion coefficient [39]. As it can be seen in equation 3.2, the depressions have a Gaussian depth profile, which can be approximated as spherical in the center.

In this model, several effects like a recoil pressure from evaporized material or energy loss because of black-body radiation are neglected. Furthermore, boundary conditions arising from the finite fiber size impacting e.g. the transverse heat conduction are not taken into account [22, 40]. Still, D. Hunger *et al* have shown that laser ablation on cleaved fiber end facets is a useful and simple way to produce fiber mirrors [8, 40]. With pulse trains containing 80 to 2400 pulses each of 0.3 W to 2 W amplitude power and 4 ms to 120 ms length, they produced mirrors with diameters between 10  $\mu\text{m}$  and 60  $\mu\text{m}$  with radii of curvature between 20  $\mu\text{m}$  and 2 000  $\mu\text{m}$ . The pulse duration as well as the power have to be chosen carefully such that the material removal occurs because of evaporation. Nevertheless, an emerging thin layer of molten silica smoothens the surface due to the surface tension, but should not lead to convex structures. In their setup, an ellipticity of a few percents was caused by an astigmatism of the laser beam and the RMS surface roughness was determined by atomic force microscopy to be  $\sigma = 0.24 \text{ nm}$ . In the course of this thesis, a more elaborate fiber shooting facility has been set up, which is discussed in the next section.

## 3.2 Production Facility

In our setup, a 9.3  $\mu\text{m}$  wavelength CO<sub>2</sub> laser<sup>2</sup> with a maximum power of 55 W is used. By setting its duty cycle to 20 %, the power is reduced to 10 W so that it is well below the damage thresholds of other setup elements after passing two 50 : 50 beamsplitters. They deflect approximately 7.5 W into beam dumps. At this duty cycle, the laser still complies with the specified power stability of  $\pm 3 \%$  [41].

The laser beam passes a magnification telescope, before it reaches an acousto-optical modulator (AOM). Afterwards, it is coupled into a hollow waveguide. The further beam path contains the outcoupling lens, phase shifting mirrors and a lens focussing the beam onto the fiber.

In the setup, the AOM and the waveguide are two components providing an advantage over conventional fiber shooting systems. These shall be further discussed below. The beam path with all the elements is depicted in figure 3.1.

---

<sup>2</sup> Coherent Diamond C55L 9.3

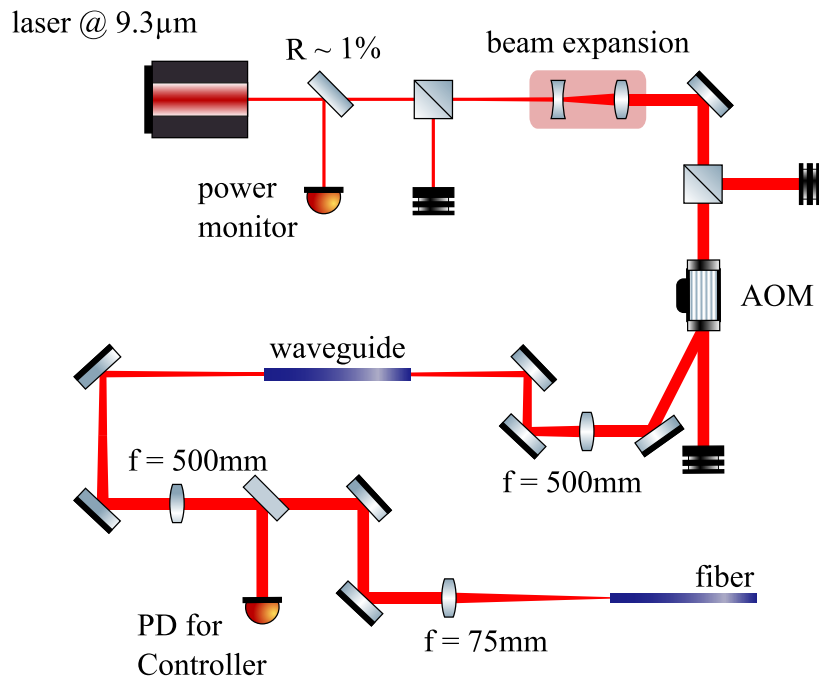


Figure 3.1: Sketch of the new fiber shooting setup.

### The Acousto-Optical Modulator

Since the wavefronts should be plane for passing this device<sup>3</sup>, the telescope is set to collimate the beam. The increased beam width also reduces the power density, protecting the AOM from damage. For the fiber shooting process, the power in the first diffraction order is used, which can be controlled by the power of the RF driving signal of the AOM. The zeroth order is dumped. The laser pulses are created by modulating the driving signal. This principle is advantageous compared to generating pulses with gates in the laser, since they would lead to significant power fluctuations.

Further improvements were made by the bachelor student Moritz Scharfstädt in stabilizing the power using a PID controller picking the reference voltage from the photodiode, which has been installed in this setup [36]. Also, the shape of the generated pulses may be adjusted in future.

### The Waveguide

To filter spatial distortions, the beam is coupled into a hollow waveguide<sup>4</sup> after passing the AOM. Its transmission can be described with  $T \propto \exp(-2L/L_d)$ , where  $L_d$  denotes the mode dependent damping length. Since  $T$  is largest for the fundamental Gaussian mode [42], the waveguide provides a "mode cleaning" effect. Furthermore, it can enhance the positional stability of its output beam.

After passing through these devices, the beam impinges onto two phase shifting mirrors. They polarize the beam circularly, since this reduces the ellipticity of the created depressions on the fiber [31]. The polarization after the mirrors was checked by rotating a temporarily installed polarizer. The degree of

<sup>3</sup> Gooch & Housego M041-11-C11V41-P5-GH77

<sup>4</sup> Laser Components HWCA1001600

polarization was determined with the minimal and maximum transmitted power to be

$$\frac{P_{\max} - P_{\min}}{P_{\max} + P_{\min}} = 0.1. \quad (3.3)$$

Afterwards, it is focussed onto the cleaved fiber tip. Around the laser focus position, the beam shape was measured via a knife-edge measurement showing a slight ellipticity and a spacial discrepancy of the waist positions by approximately  $150 \mu\text{m}$  (see figure 3.2).

After this introduction into the fiber production setup the different shooting techniques will be discussed.

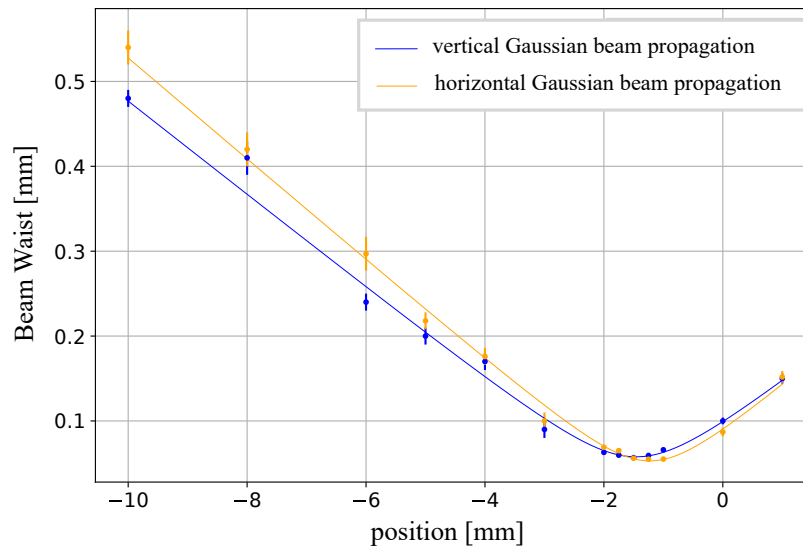


Figure 3.2: This figure shows the beam widths around the waist of the laser beam measured with the knife-edge method. A low ellipticity due to a slight mismatch of the waist positions is ascertainable. The image is taken from [36].

### 3.3 Shooting Technique

For producing fiber mirrors, different ways of applying pulses can be used. The old setup, that existed in our group, used the simple method is to expose the fiber tip to a single pulse train targeting the center of the fiber end facet. In this case, the mirror diameters and radii of curvature are limited in size and beam ellipticities directly translate into deviations from the ideal Gaussian crater shape [40].

The new setup provides a precise beam pointing stability that enables using the dot milling technique [36], which was developed by K. Ott *et al* (illustrated in figure 3.3) [29]. This technique also requires precise positioning of the fiber with respect to the beam not only parallel to the fiber surface, but also to move it into or out of focus. This is realized by mounting the fibers on a 3-axis translation stage<sup>5</sup> [36] with a precision of 300 nm after 500 ms settling time.

Limitations in mirror diameters and depth have not been observed, since an arbitrary number of circles

<sup>5</sup> Aerotech ANT95-L Nanopositioning Stage

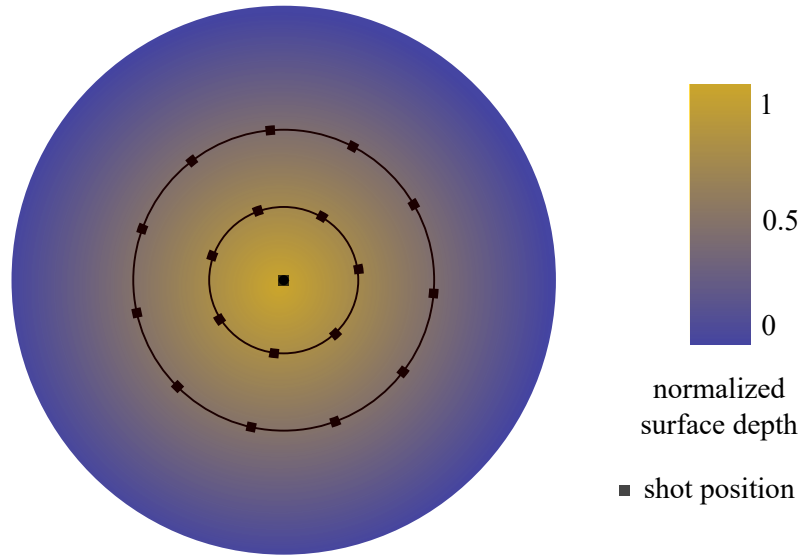


Figure 3.3: This figure illustrates the dot milling technique by showing a cleaved surface of a fiber end facet with concentric circles, along which craters are distributed by single pulses. The distance between neighboring depressions has to be small enough so that the overlap of all craters forms one depression. One begins with shooting the hollows of the outermost circle and goes further to the circles inside. While shooting the depressions within one circle, every second one is postponed to give the material time to resolidify, before the next pulse occurs in the same area. At the end, a single shot in the center is given not only to shape the central region, but also to give the whole structure a Gaussian shape and smoothen remaining ripples [29].

with an optional number of shots can be used giving a large number of possible configurations. Although good results were obtained, there is still room for improvement: Single pulses with different power or pulse trains can be used for creating each depression. Also mirrors with controlled elliptical shape may be produced by replacing the circles by ellipses to built dual wavelength cavities [43].

The main operator of this setup was P. Fürtjes, who produced a large number of fiber mirrors. For completeness, her results obtained with this setup and the way how they are recieved are shortly described in the following sections.

### 3.4 Surface Reconstruction

To obtain a 3D-profile of the created structure, a scanning white light interferometer is used, which has already been set up in an earlier master thesis (see figure 3.4) [22]. The light of a halogen bulb passes a color filter, before it illuminates a pinhole, which serves as a light source for a Mirau objective. The coherence length  $l_{\text{coh}}$  of the light is of approximately  $1 \mu\text{m}$ . Within the objective, the light impinges on a partially reflecting mirror splitting the light into two beams. One is focussed onto the fiber end facet and is reflected back into the objective. It creates an interference pattern with the other beam, which covers a fixed pathlength given by the interferometer geometry [44]. The objective is mounted on a piezo translation stage in order to position it with a precision of 5 nm. By moving the objective with respect to the probe, the length difference between the paths, that are depicted in figure 3.5 as red and green, is

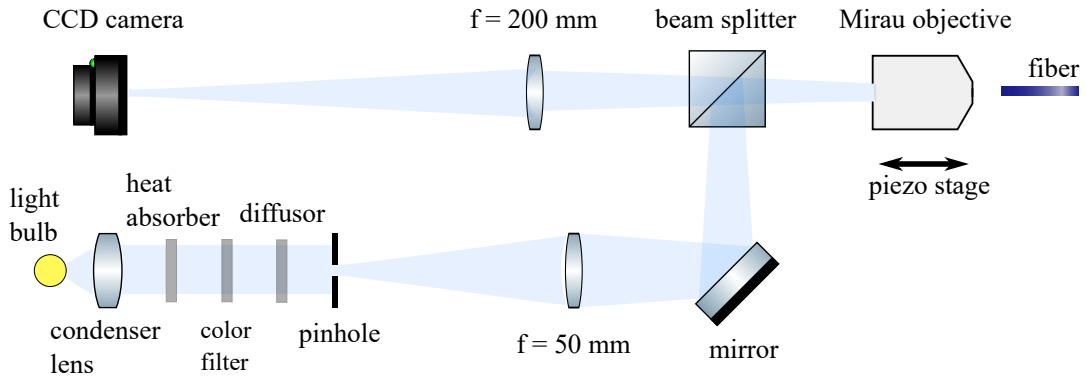


Figure 3.4: This figure shows the complete interferometer setup. The bulb light is collimated by a condenser and travels through a heat absorber and a color filter to prevent the setup from heating up and give the light the desired spectrum, which determines  $l_{\text{coh}}$ . A diffusor improves the image quality by blurring image patterns arising from structures of the bulb. The subsequent 4 mm diameter pinhole acts as the interferometer light source. A beam splitter is used as a partially reflecting mirror to deflect light into the objective and let the image fall onto the CCD camera. The image is taken from Michael Kubista.

changed. For different objective heights  $z$  (see figure 3.5) the interference pattern recorded by one pixel

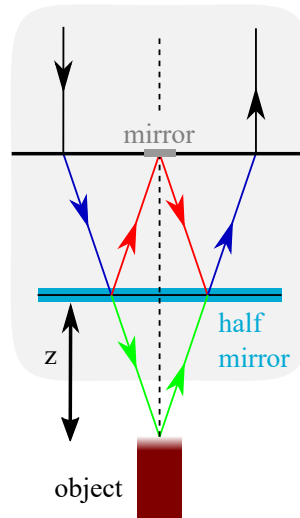


Figure 3.5: This figure shows the light paths in a Mirau objective. The image is adapted from [22].

of the CCD camera takes the form of

$$I = I_0 + \exp \left\{ -4 \left( \frac{z - z_0}{l_{\text{coh}}} \right)^2 \right\} \cos \left( 4\pi \frac{z - z_0}{\lambda_0} - \phi_0 \right), \quad (3.4)$$

where  $z_0$  denotes the objective height with vanishing path difference [45]. Extracting  $z_0$  for every pixel yields a complete 3D surface reconstruction. To retrieve information about the mirror geometry, such as radius of curvature, depression depth and diameter, a Gaussian and a spherical function is fitted to the

central region of the structure.

### 3.5 Obtained Structures

Due to the high versatility of the fiber shooting setup limitations in diameter or depth size could not be observed yet. Ellipticities defined as

$$\epsilon = (R_{\max} - R_{\min}) / (R_{\max} + R_{\min}) \quad (3.5)$$

could be reduced to values on the order of 1%. The reconstruction of a typical mirror geometry can be seen in figure 3.6. The surface roughness could not be determined, since methods with a similar precision compared to atomic force microscopy were not available. By applying a high reflectivity coating consisting of alternating layers of  $\text{SiO}_2$  and  $\text{Ta}_2\text{O}_5$ , the carved fiber end facets become Bragg mirrors. The number of layers determines the transmittance, which for our purposes is set into the regime of several 10 ppm. After the coating is applied, the fiber mirrors are ready to form a cavity.

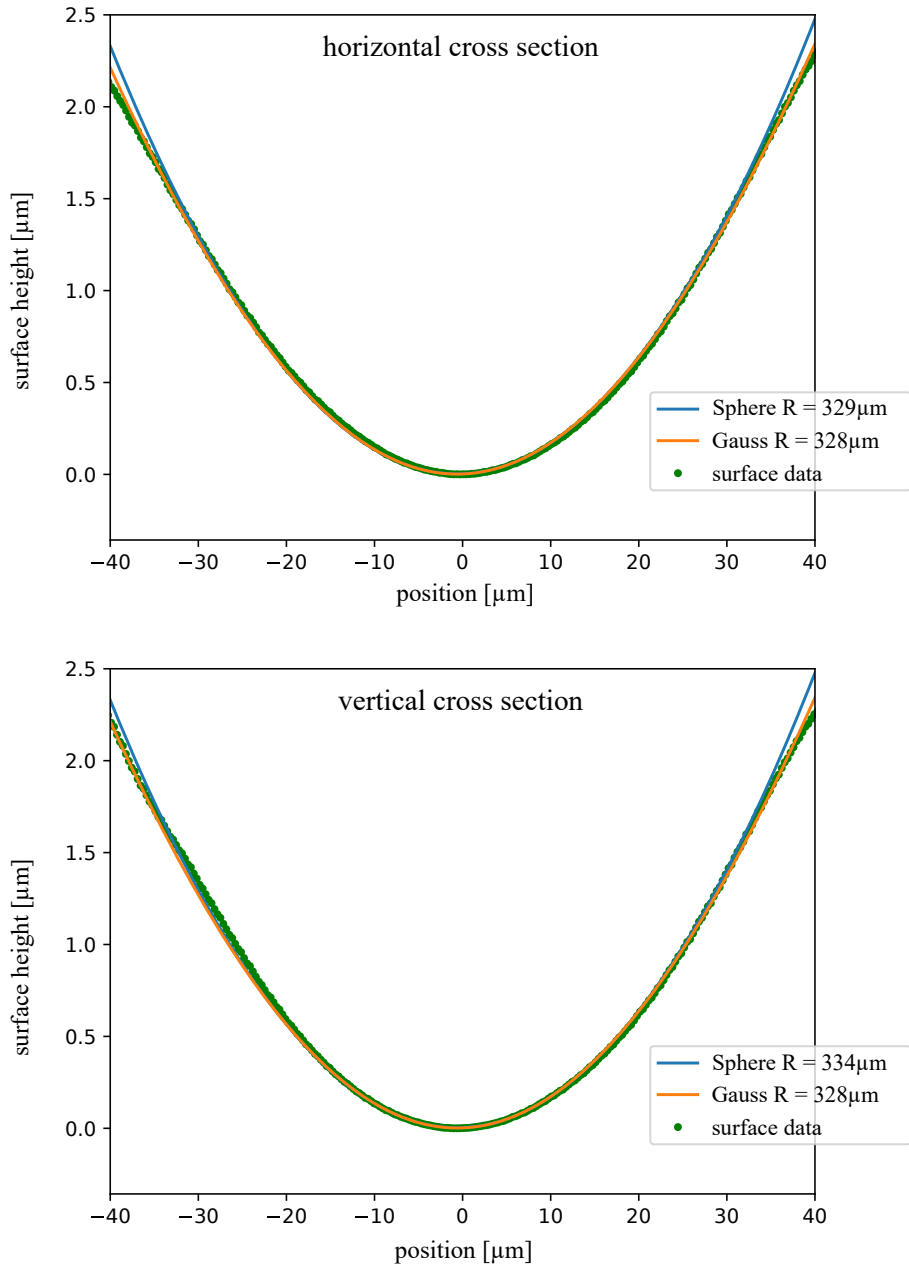


Figure 3.6: This figure shows the reconstructed cross-section in horizontal and vertical axis as well as the Gaussian and spherical fit with their corresponding radii of curvature. An excellent agreement between the radii of curvature is noticeable. The conformity of the parameters in horizontal and vertical direction indicates a low ellipticity. The image is taken from [36].

---

## Fiber Fabry-Perot Cavity Assembly

---

In this chapter, the construction of a fiber Fabry-Perot cavity and its characterization is described. An alignment setup has been assembled, which was used for building a particular fiber cavity system. Its design follows the one, which was set up by J. Gallego [6]. The setup consists of an optical as well as a mechanical part for fiber mirror alignment with in-situ line shape observation.

In the following section, the optical part of the alignment setup is presented.

### 4.1 Optical Setup for Cavity Lineshape Observation

In order to build a cavity with the specific properties, it is necessary to extract information about the coupling efficiency, the finesse (section 2.2) and polarization splitting (section 2.2.2). For this purpose, an optical setup (see figure 4.1) has been built, with which these properties can be observed. When following the optical path depicted in figure 4.1, the laser beam first travels through a Faraday isolator shielding against back reflection. After this, it is coupled into a polarization maintaining fiber to mode clean the beam and meanwhile keep its well defined linear polarization. A half-wave plate and a polarizing beamsplitter (PBS) directs the light through an AOM in double-pass configuration, which is driven with a radiofrequency signal at 80 MHz. The alignment is done such that two beams with frequencies of  $\omega_0$  and  $\omega_0 + 2 \cdot 80$  MHz overlap and continue on the path reflected from the PBS.

A half-wave plate and a polarizer can be used for controlling the intensity, before the beam passes a combination of a PBS, two quarter-wave and one half-wave plate. Subsequently, it is coupled into a fiber mirror. Thereby, the polarization can be manipulated such that the reflected beam from the fiber mirror has a polarization turned by  $90^\circ$  after passing the wave plates again. After being reflected from the PBS, the beam hits a photodiode. Its signal passes a band stop filter, which filters the beat signal at 160 MHz. With this wave plate setup, the polarization of the excited cavity mode is circular, meaning that two perpendicular linear components are present. This allows the detection of polarization dependent resonator mode splittings (see section 2.2.2).

When scanning the cavity length over the resonance, two dips in the reflection signal are detected because of the generated sideband. The photodiode in transmission direction recognizes peaks, respectively. The technique to extract information about the coupling efficiency of the fiber mode into the cavity and its finesse is presented in the following section.

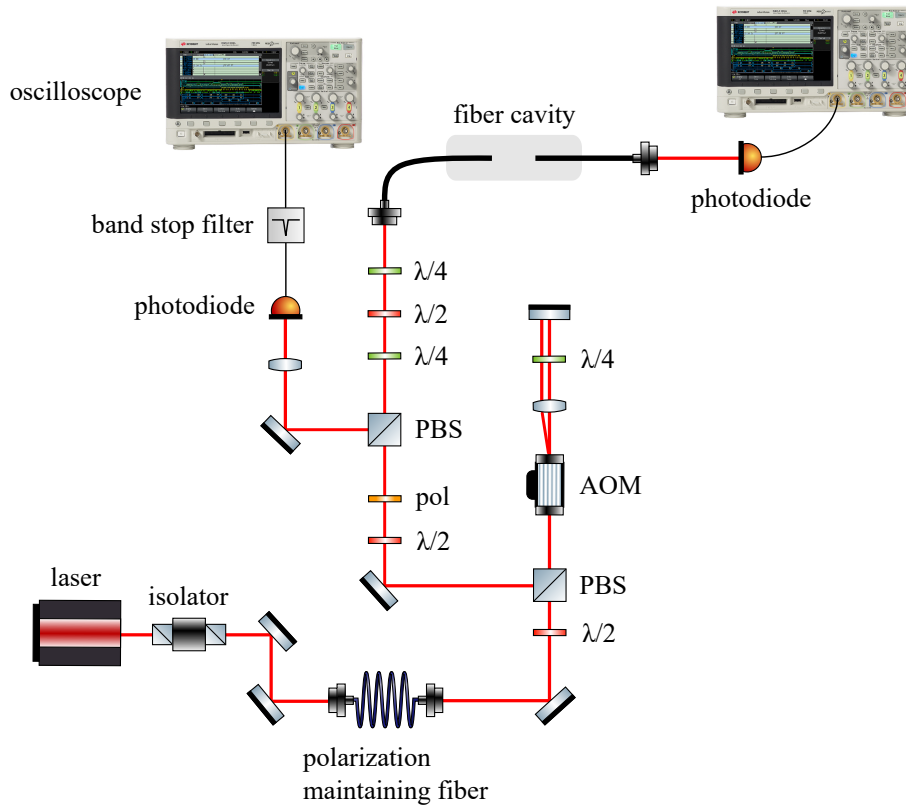


Figure 4.1: Optical setup for cavity alignment and lineshape observation.

## 4.2 Observing the Cavity Resonance

This section focusses on the information obtained by the measurement of the reflected signal, since this signal allows to retrieve information about the incoupling efficiency into the cavity. However, a transmission signal of the built cavity could not be observed due to high losses the transmission fiber, which can result from a large mirror decentration or a waveguide damage. The cause has not been further investigated.

### 4.2.1 Cavity Line Shape from Reflection Measurement

To observe the cavity line shape, it is necessary either to scan the laser frequency or the cavity length. The measurements presented below are performed with the cavity, which has been built in the course of this research work. Its design is introduced in the following section. By applying a triangular voltage to a shear piezo, the mirror distance of this cavity can be scanned. A typical observation in reflection direction is shown in figure 4.3. Two dips are visible, which correspond to the first and second order of the AOM. As it is shown in section 2.2.3, the line shape can be described by the superimposition of a Lorentzian and a dispersive term. A sum of two such functions with a linear background is fitted to the obtained data. From this fit, the time scale of the oscilloscope is calibrated to frequencies, as the time difference of both Lorentzian peaks corresponds to 160 MHz. To determine the Lorentzian width, the AOM is switched off and a single resonance is fitted (see also figure 4.3). The scan properties, defined by

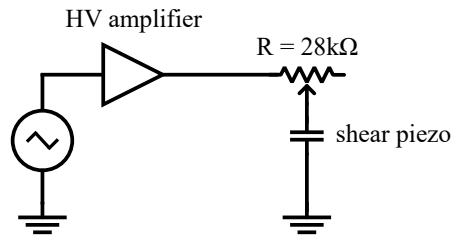


Figure 4.2: Electrical circuit for piezo high voltage supply.

the amplitude and frequency of an amplified triangular voltage, remain the same for both measurements. During the first attempts to use this technique, the signal was too unstable to obtain reliable data. It could be stabilized by connecting a variable resistor in series to the shear piezo, which acts together with the piezo capacity as a low pass filtering RC element (see figure 4.2). At a resistance of 28 k $\Omega$ , the fluctuations vanish. A possible reason is a jitter of the piezo induced by high-frequency noise on the supply voltage, driving a harmonic of a resonance frequency. Despite this, there are also other noise sources: If low scan frequencies < 50 hertz are used, the measurement becomes sensitive to mechanical vibrations of macroscopic objects on the optical table. At high frequencies, the lineshape gets distorted by an interference effect between the light reflected at the fiber tip and the decaying intra-cavity field. For calculating the finesse, the free-spectral range is determined by measuring the mirror distance with a microscope and using formula 2.6.

#### 4.2.2 Obtained Finesse

Several finesse measurements have been performed with different scan frequencies, but same amplitudes (see figure 4.4). The most reliable data is obtained with scan frequencies of 120 Hz and 160 Hz (marked in green), since it is not affected by the low-frequency noise. Still, the scan is slow enough to avoid the interference (see the last section). The shown error bars display the  $1\sigma$  environment resulting from the fit. The real uncertainty is influenced by systematic effects and is further investigated in the work of Carlos Saavedra. The average of both trustable values gives a finesse of approximately 88 000. In contrast to the finesse measurement, the coupling efficiencies determined by the ratio of the Lorentzian peak height to the background seem to be independent of the scan frequency. The obtained value is  $(31.19 \pm 0.11) \%$ .

### 4.3 Cavity Assembly Steps

In order to get a better understanding, it might be helpful for the reader to take a closer look at figure 4.5. This figure shows a sketch of the final assembly. The different numbers, by which the components are labeled in the following section, are also assigned in the figure.

In the first step a shear piezo (1), which allows to lock and scan the cavity length over  $\pm 1.5 \mu\text{m}$  with a rate of up to 500 Hz, is glued to a T-piece (2) made of Macor, which is an ultra-high vacuum compatible ceramic. This T-piece allows to screw the holder to alignment stages and will later act as a spacer. A V-groove (3) made of the same material is glued to the other side of the piezo allowing a stable fiber positioning. To do so, thermally curing adhesive is used so that the pieces have to be baked for approximately four hours at  $100^\circ\text{C}$  in an oven [46].

Kapton isolated copper wires (4) ensure the electrical connection to the piezo. These wires are agglu-

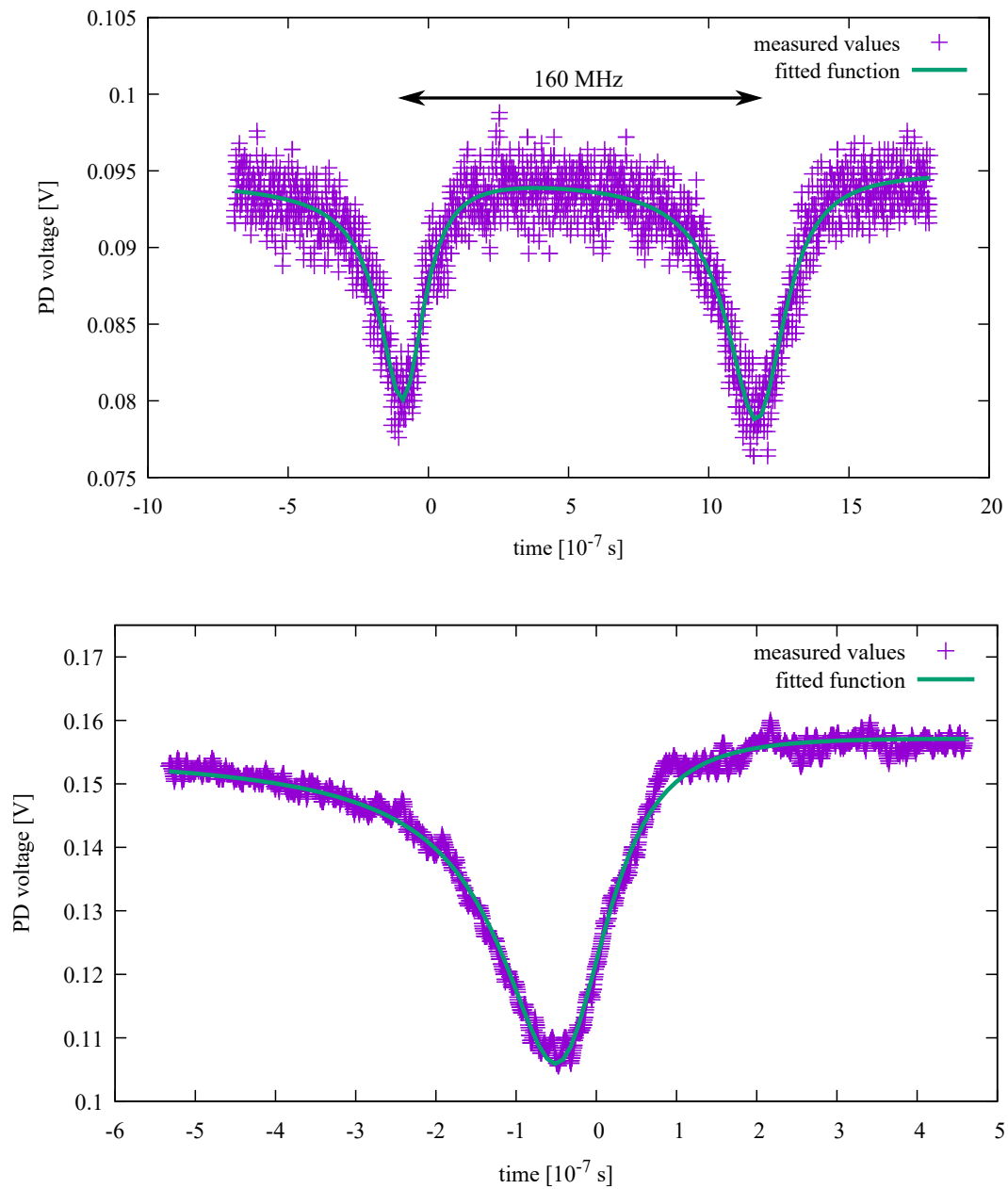


Figure 4.3: This figure shows measurement data to determine the resonance width and finesse with a scan frequency of 120 Hz.

- a): Due to the AOM, two resonances are measured. Their "time distance" corresponds to twice the RF driving frequency.
- b): Since the AOM may induce distortions measurements, it is switched off for measuring the resonance width.

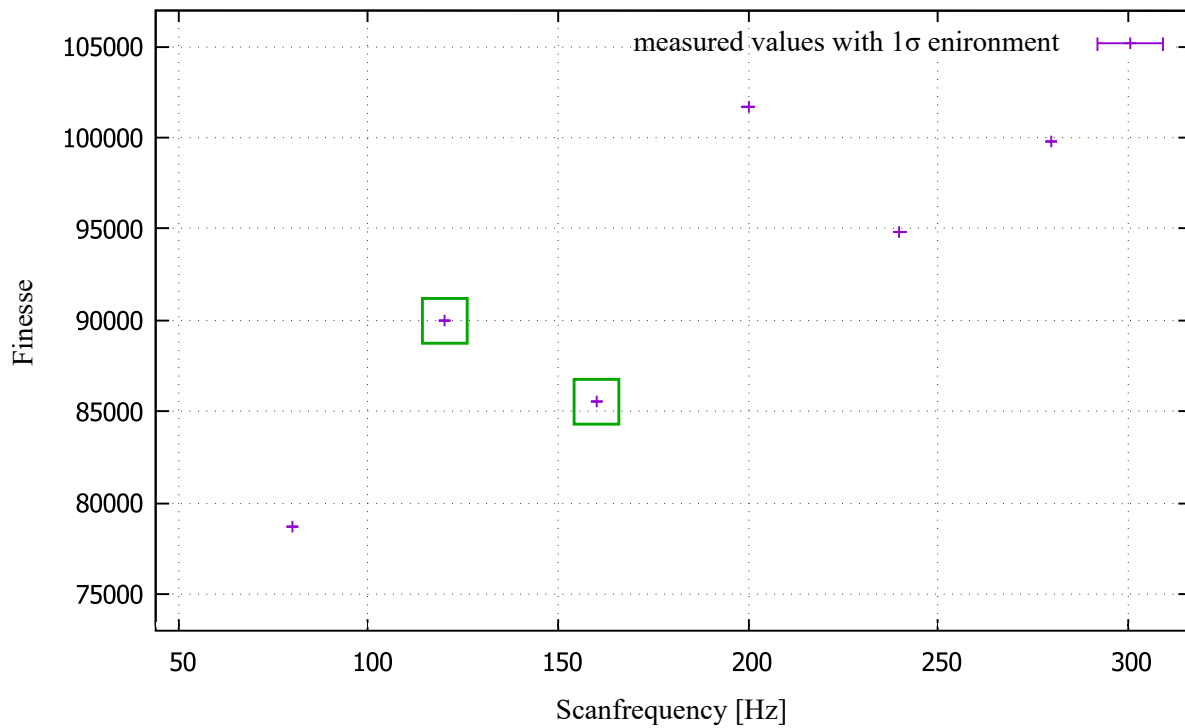


Figure 4.4: Estimated finesse values for different scan frequencies. The errors denoting the  $1\sigma$  uncertainty are solely given by the fit and are on the order of 4 %, so that the errorbars are hardly visible.

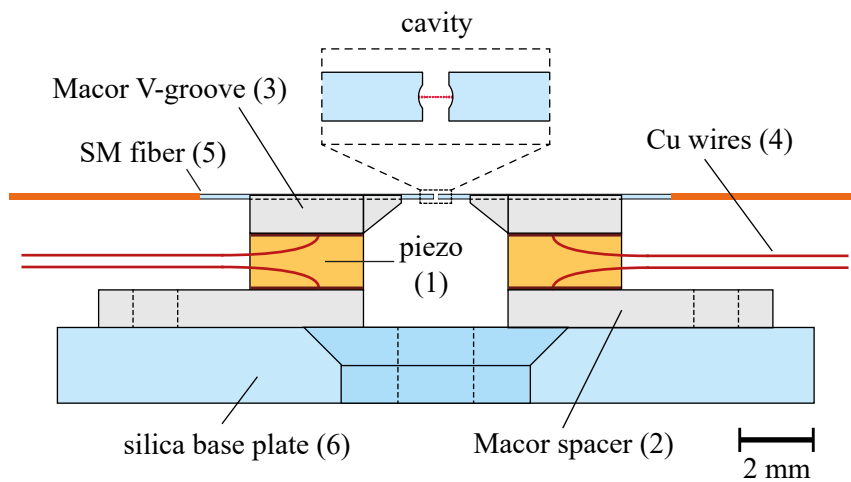


Figure 4.5: This figure shows a sketch of the cavity design. The image is adapted from [18].

tinated with conducting silver glue, which hardens for 5 hours at a temperature of also  $100^\circ$  [47]. An example of this construction can be found in figure 4.6.



Figure 4.6: This figure shows the construction of the T-piece (below), the shear piezo (middle) and the V-groove (top), in which the fiber is placed for the cavity assembly.

For alignment, the T-pieces are screwed to stages and the fiber mirrors (5) are placed in their respective groove. One stage is a three-axis translation stage with a fiber rotator, by which the fiber is turned around its axis. This device allows the control over the polarization dependent mode splitting arising from the ellipticity of the fiber mirrors (see section 2.2.2) [31]. The other stage is a two-axis rotation stage enabling the positional optimization of the remaining two degrees of freedom. The curvature of the fiber mirrors, that are in stock, is designed for a concentric cavity with a length of  $90\ \mu\text{m}$ .

By observing the fiber tips with microscopes, their distance can be brought to the desired length with a precision of  $\pm 2\ \mu\text{m}$ . The fine adjustment including setting the optimal length and removing polarization splitting as well as angles between the fiber mirrors is done by observing the lineshape. The optimal setting is found, when higher order transversal modes are removed from the cavity spectrum (see section 2.2.2) and the amplitude of the remaining resonance dip indicates a maximum coupling to the ground mode. Subsequently, the T-pieces are stuck to a common silica base-plate (6). While the glue hardens, positional shifts can occur so that the cavity may have to be realigned during the curing process. The base-plate is equipped with a hole, that has to be positioned under the cavity for optical access. In this step, a glue is used, that is partially cured by applying UV light. Within 24 hours it has to be brought into a vacuum system, which has been built in the course of the research work for this thesis [48]. It is further explained in the following section.

## 4.4 Vacuum System

As the produced cavities have to be ultra-high vacuum compatible, it is highly important to prevent the adhesive from outgassing in the vacuum. For this purpose, a test vacuum system has been set up, which is pumped by two turbopumps to a pressure of  $6 \times 10^{-8}$  mbar. A bake-out has not been done yet. It will be performed, when the next built cavity is placed inside. A sketch of the system can be found in figure 4.7. It provides electrical as well as fiber feedthroughs to allow continuous measurement of the finesse. In the future, it can also be used for testing environmental influences on the finesse. This is of high interest, since a finesse degradation in vacuum is reported from several experiments, including our FCQED experiment [6]. In the setup, one pipe is intentionally closed with a blank flange leaving the possibility to install a vaporized rubidium source. By doing so, the current environment in the FCQED experiment can be recreated. Two viewports are already installed giving the possibility to estimate the Rubidium concentration for example by absorption spectroscopy.

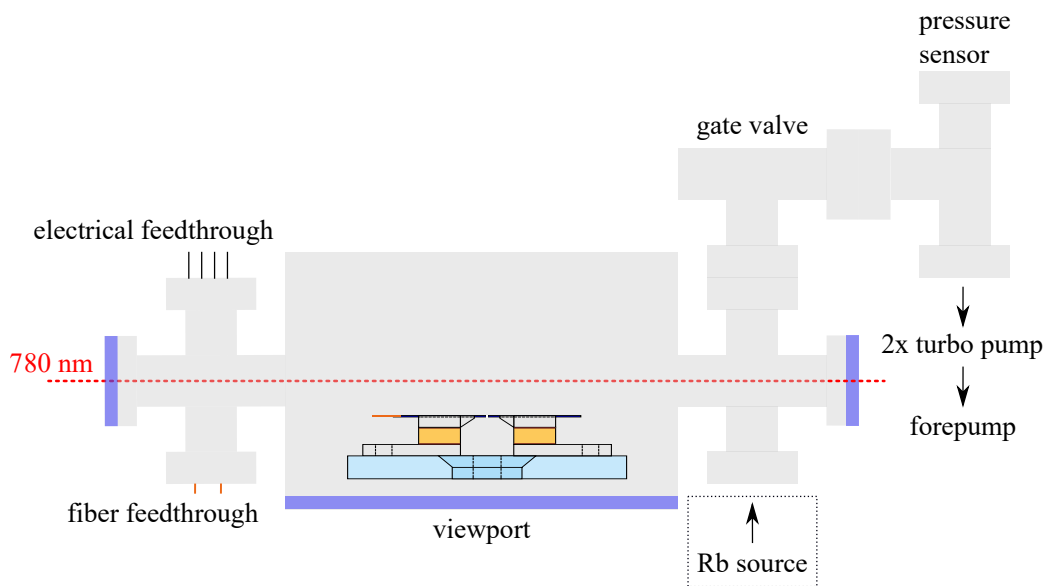


Figure 4.7: This figure shows a sketch of the assembled vacuum system for glue curing. In the future, it can be extended with a rubidium source to investigate the cause of finesse degradations.

Strong indications have been found that oxygen depletion in the outermost  $\text{Ta}_2\text{O}_5$  coating layer is the primary origin of a mirror quality degradation [49]. This was investigated and confirmed by X-ray photoelectron spectroscopy measurements as presented in [33]. However, other groups, as the one of J. Reichel, do not experience a finesse decrease. This is why it has to be carefully analyzed in our system. A method to possibly cure oxygen depletion by annealing is presented in the following section.

## 4.5 Annealing Process

One way to enhance the quality of high reflectivity coatings, such as  $\text{SiO}_2$  and  $\text{Ta}_2\text{O}_5$ , is to cure them thermally. For this purpose, the fiber ends are heated for several hours. The annealing for the built cavity was performed for 5 h at a temperature of  $400^\circ$ .

It has been shown that this process leads to a homogenization of oxide layers and therefore reduces scattering losses in the mirrors, which are directly connected to the surface roughness [33]. J. Gallego presented measurements, according to which the transmission coefficient rises on the order of a few 10 ppm [6].

This effect is reversible, as shown by B. Brandstätter *et al.* They measured an increase of the finesse, when the fibers are annealed in air, and a decrease, when they are annealed in vacuum leading to oxygen depletion [33].

A test series, on how the finesse changes with the annealing temperature and its discussion, has been performed by the bachelor student H. Nienhaus and can be found in [50].



---

## Enhancing the Mode-Matching of Fiber Fabry-Perot Cavities

---

As it has been discussed in section 2.2.3, the spatial overlap of light in single-mode fibers and large symmetric cavities can become critically low. Thus, mode-matching optics shall be applied to fiber cavities by launching the light of a single-mode fiber through a GRIN fiber lens into a multi-mode fiber serving as a mirror substrate [14]. An illustration can be found in figure 5.1.

This technique is realized with a "splice and cut" approach: First, the single mode fiber is spliced to a long piece of GRIN fiber, which is then cleaved to a length such that the desired output mode exits the later fiber assembly. As a second step, a multi-mode fiber is spliced to this GRIN lens, which is cleaved at a distance, which determines the cavity length.

### 5.1 Choice of Fiber

As it is shown in section 2.1.2, GRIN fibers can have defective refractive index profiles, which lead to strong optical aberrations. Since the resulting beam profile distortions would lower the coupling efficiency, the fibers have to be chosen carefully for this project. Although the manufacturers mostly keep information about their fibers secretly, the following GRIN fibers were selected:

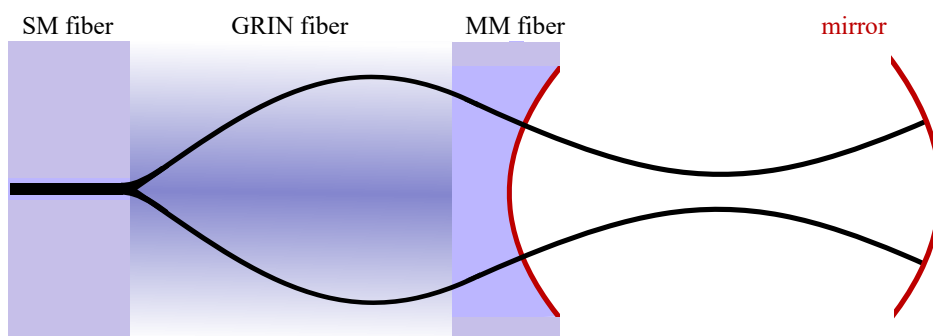


Figure 5.1: This figure shows the approach to install mode-matching optics into fiber cavity assemblies. The laser light is mode cleaned in a single-mode fiber, before its mode is converted by GRIN fiber lens. The mirror is machined onto a piece of multi-mode fiber.

### Thorlabs GIF625

The GIF625 fiber, which is distributed by Thorlabs, has a core diameter of  $62.5\ \mu\text{m}$  and is the only fiber, from which information about the index profile could be obtained. Lorensen *et al* received manufacturer specifications in 2013, from which they obtained the exponent of  $(r/a)$  to be  $\alpha = 1.96$ . This is the value closest to 2 among the fibers, they have characterized (see section 2.1.2). They did not notice ripples or a central index dip and they suggest this fiber to be used in optical coherence tomography [26].

From their data, its refocussing length is calculated to be  $500\ \mu\text{m}$ .

### OFS BF04432-1

Although there is no information available about the index profile of this fiber, the G.K. Gulati *et al* used this fiber as the focusing element for their mode-matched cavities [14]. Since the core diameter is  $100\ \mu\text{m}$ , the refocussing length is expected to be much longer, but exact data on this could not be obtained yet.

### Corning InfiniCor 300

The InfiniCor is a low-priced GRIN fiber from Corning, which is used for producing different fiber optic probes by various companies<sup>1</sup>. It has a core diameter of  $62.5\ \mu\text{m}$ , but there is no further information on the index profile available.

As the endpiece multi-mode waveguide, the FG105LCA fiber, distributed by Thorlabs, was chosen because of its large pure silica core with  $105\ \mu\text{m}$  diameter. This promises the most reproducible results during fiber shooting.

The cleaving and splicing process has been optimized for these fibers, which is discussed below.

## 5.2 Fiber Cleaving

The term cleaving denotes the controlled breaking of fibers aiming for a flat end surface perpendicular to the fiber axis. As a first step, the fiber is tightened with a force, which is set with a precision better than  $0.1\ \text{N}$ . Then, a blade hits the side of the tensioned fiber such that the resulting crack propagates through the glass in a controlled way, eventually cutting it into two pieces. Therefore, the cleave tension has to be optimized to obtain high-quality surfaces for splicing and the later fiber shooting. Further, controlling the cleave length with a precision of approximately  $\pm 10\ \mu\text{m}$  is indispensable, since this directly influences the focal length of the GRIN fiber lens and thereby the cavity mode.

In the following section, the influence of the cleave tension is further discussed, before the cleave length control setup is introduced.

### 5.2.1 Cleave Tension

The cleave tension directly influences the propagation of the initial crack, which is scribed with the cleave blade. Thus, four regions on the fiber end facet arise.

The first region is determined by the spot, where the blade hits the fiber. The point of crack initiation typically shows unevennesses of about  $500\ \text{nm}$  minoring the cleave quality. Around this point, an optically smooth region arises, as the crack propagates across the fiber. As it goes further away from the initiation site, it forks up into multiple crack fronts causing the hackle region characterized by ripple amplitudes of a few  $100\ \text{nm}$ . The mist region, as it is shown in figure 5.2, is a transition between the smooth and the

---

<sup>1</sup> e.g. fionec GmbH

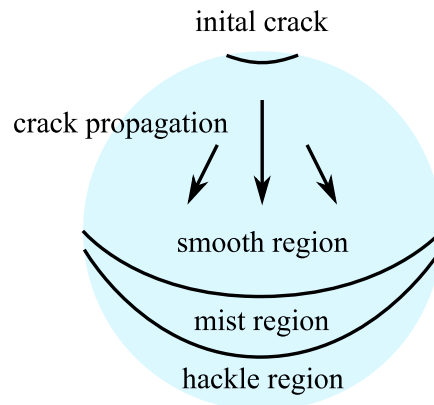


Figure 5.2: This figure illustrates structural areas typically arising from unfavorable cleave tensions. The image is adapted from [51].

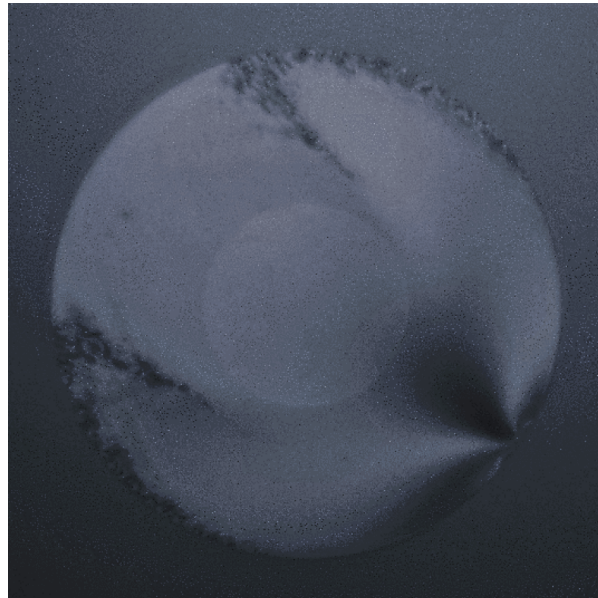


Figure 5.3: This figure shows an interferogram of a fiber cleaved with a too strong tension taken with the microscope introduced in section 3.4. On the lower right, the position of the blade impact and on the top and left the hackle is can be seen. The image is taken from [36].

hackle region [51]. An interferogram of a fiber end facet with hackle is shown in figure 5.3.

The hackle area can be minimized by lowering the cleave tension, as long as the fiber does not bend, when the blade hits. Such a bending would cause large cleave angles and may even induce a significant wearing of the blade.

Typical clamping forces are around 2.2 N for the used single-mode fibers. For GRIN and multi-mode fibers, the cleave tension is lowered to 1.9 N.

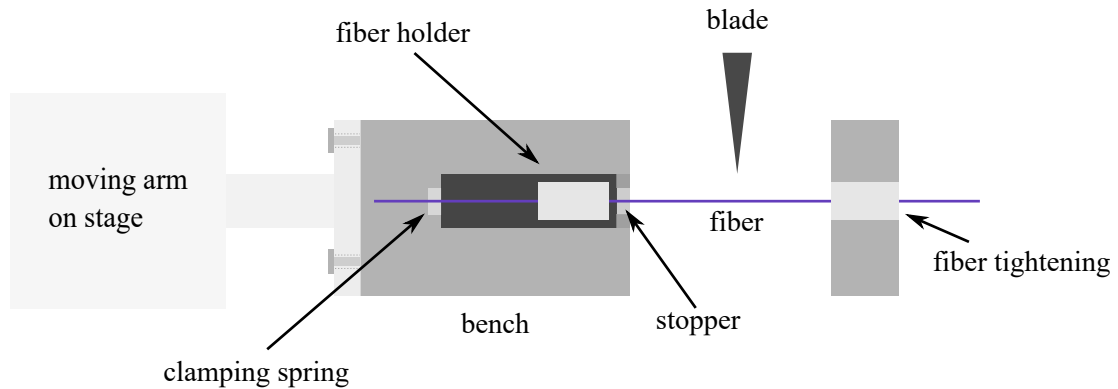


Figure 5.4: This figure illustrates the cleaver setup for cleave length control.

### 5.2.2 Cleave Length Control

To make use of a mode-matching lens integration into a fiber cavity assembly, it is essential to have control over its focal length. In the case of GRIN fiber-based focussing, it has to be ensured that its length can be set with a precision of a few  $\mu\text{m}$ .

For implementing this in our fiber assembly procedure, the launching fiber is clamped in a fiber holder<sup>2</sup>, where it will stay during the whole cleaving and splicing process. The holder is then fixed on a moveable bench in the cleaver, on which it is precisely held by a spring pushing it against a stopper (see figure 5.4). The bench itself is screwed via a specially designed arm to an aligning micrometer stage. By moving this bench with the stage, the cleave length is adjusted. This movement is observed with a high-magnification USB microscope<sup>3</sup> to precisely adjust the travel distance. During a cleave, the bench is also screwed to the cleaver housing to provide more stability, when the cleave tension is applied. After the cleaving process, the fiber is spliced to a second fiber. After inserting the fiber assembly back into the cleaver, the final length of the second fiber is set by moving the micrometer stage, before the next cleave is applied. This procedure gives the possibility to connect a precisely defined GRIN fiber lens to a single-mode fiber and then to link it to a multi-mode fiber. The length control works with a reproducibility of well below  $5\ \mu\text{m}$ , which is shown in figure 5.5. The splicing technique is discussed in the following section.

### 5.3 Fusion Splicing

Fusion splicing is a welding process, by which two optical fibers are connected such that a permanent joint is formed, which can exhibit high mechanical strength and therefore long-term reliability.

Depending on the fiber types and the nature of the splice the optical transmission losses can be on the order of 0.3 dB and lower [51]. Other splice methods, like mechanical splices, are disadvantageous, as they provide joint cross sections, which are much larger than the fiber itself. This makes the fusion splicing technique the optimal solution to achieve mode-matching in fiber cavities<sup>4</sup>.

In the following section, the procedure is explained, before the optimization of the splicing process for the used fibers is discussed.

<sup>2</sup> Fujikura FH-100series

<sup>3</sup> Dino-Lite AM4113T5

<sup>4</sup> Recently companies introduced splicers based on the absorption of  $\text{CO}_2$  laser light in fused silica. This technique may be advantageous, but is also highly expensive.

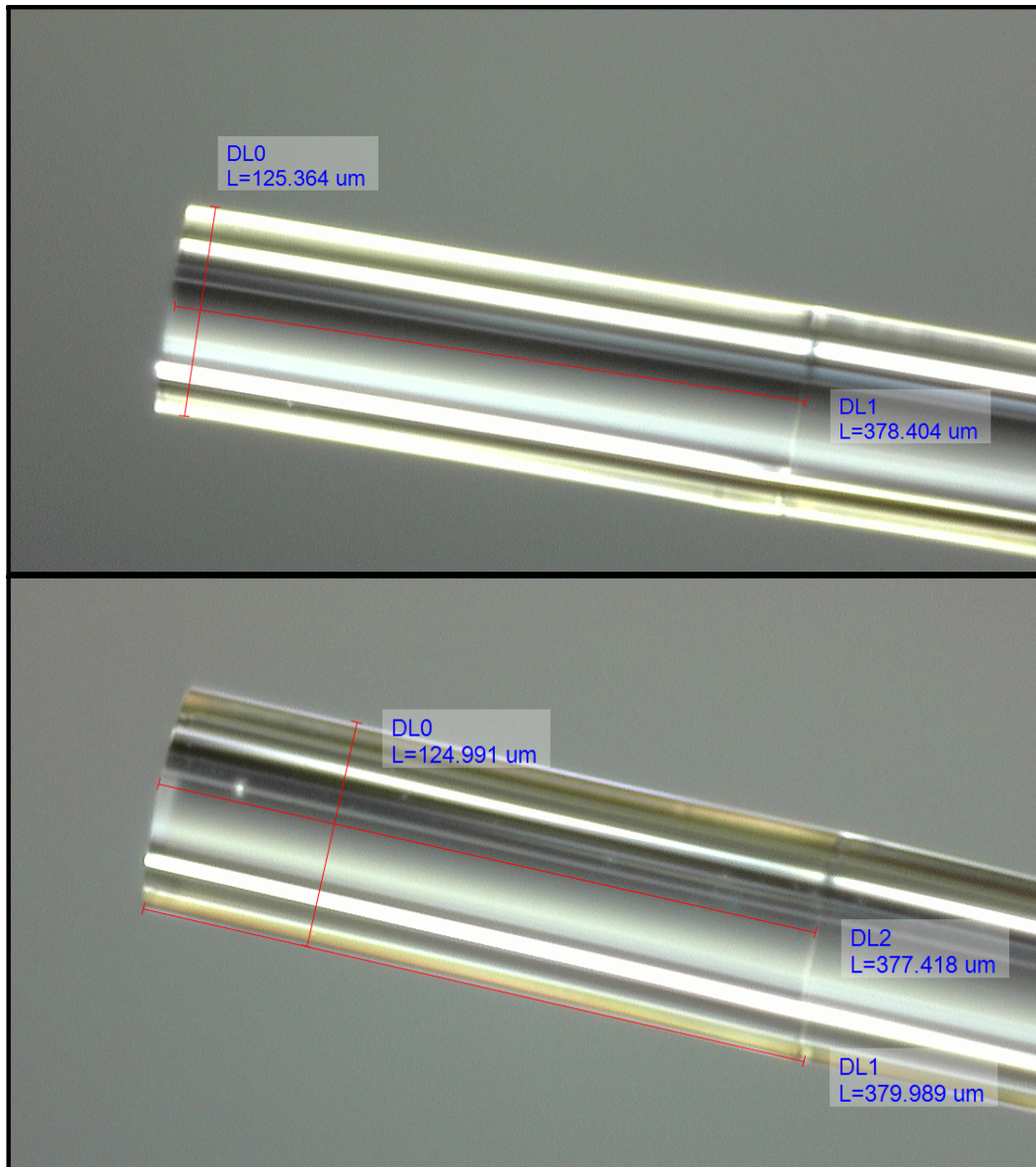


Figure 5.5: This figure illustrates the reproducibility of cleave lengths by showing two examples. Deviations at the given setting of  $380\ \mu\text{m}$  are less than  $3\ \mu\text{m}$ . The length calibration is done by measuring the fiber diameter, which is specified as  $(125 \pm 1)\ \mu\text{m}$ . Due to the finite size of the white colored joint region, discrepancies of the length measurements are expected. Due to the narrow joint region, they are well below  $5\ \mu\text{m}$ .

### 5.3.1 Splice Procedure

The fusion splicing machine used for this project is a fully automatized fusion splicer<sup>5</sup>. The description of the different alignment steps follows the procedure of this specific splicer [52] so that it may differ from the procedures of other splicers.

After the fiber holders with their respective fiber are placed in the splicer, it begins with a pre-alignment procedure, where the fiber tips are moved towards each other, until their distance is close enough to perform a cleaning arc. This cleaning arc burns dust and solvent residuals with adjustable arc time and power.

Angles of the fibers with respect to each other as well as the end facet quality are then measured with two inbuilt microscopes. The cleave angle as well as the fiber angles are displayed and an error message occurs, if the angles are larger than  $0.3^\circ$ . Typical fiber angles are below  $0.1^\circ$ .

In a second step, the fibers are aligned according to the preset values (see figure 5.6): The gap between the fibers can be varied between a few and several hundred  $\mu\text{m}$ . Additionally, the gap center can be shifted with respect to the electrodes. In doing so, the relative exposure to the heating arcs and therefore the relative temperature can be tuned.

Fiber decentrations, as shown in figure 5.6, are measured by the splicer and are typically lower than 100 nm.

Before the splicing starts, the fiber ends are heated up by a prefuse, where the following parameters have been varied:

- prefuse time meaning the complete time duration needed for the preheating,
- prefuse on- and off-times for pulsed arcs during the prefuse and the
- arc power referring to the amplitude in case of pulsed arcs.

After preheating, the arc discharge continues, while the fiber tips are moved together and start overlapping by  $10\ \mu\text{m}$  to  $30\ \mu\text{m}$  depending on the fiber type. When they come into contact, the main arc is fired, which can be controlled analogously to the prefuse by the main arc time and its power. Here, only continuous arcing is possible.

The parameters as mentioned earlier have to be optimized for every fiber type. Since the splicer is not developed for handling GRIN fibers and it is more difficult to splice fibers with different geometries, new splice programmes had to be found, which are presented in the following section.

### 5.3.2 Optimizing Splice Settings

The parameters introduced in section 5.3.1 have to be adapted according to the specific fibers such that the fiber material softens to form a homogeneous joint, but does not liquify. The softening point depends crucially on the dopant material and its concentration. The core of the used GRIN fibers is strongly doped with germanium dioxide providing a softening point of  $615\ ^\circ\text{C}$  [53], which is much lower compared to fused silica with  $1720\ ^\circ\text{C}$  [54]. The cladding of the used multi-mode fiber is doped with fluorine, which in contrast to germanium may undergo a significant diffusion process, when it is heated up [51].

Nevertheless, a region of inner-structural collapse due to high temperatures is unavoidable with fusion splicing and has a length of up to  $100\ \mu\text{m}$  [51].

As any kind of structural changes and losses contribute to mode deterioration, it is necessary to optimize the settings. The appearance of strong material deformations, as shown in figure 5.7, can be reduced

---

<sup>5</sup> Fujikura ARCMaster FSM-100P+

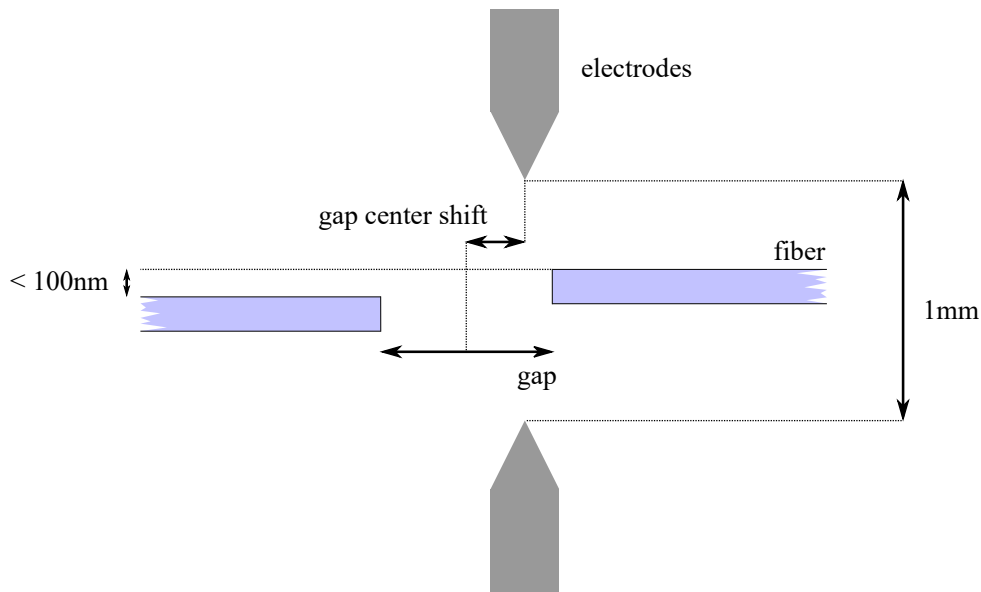


Figure 5.6: This figure illustrates the fiber alignment inside the fusion splicer used for this project. Among others the gap between the fibers and the position of the gap center are adjustable. Displacements of the fibers with respect to each other are less than 100 nm.

by changing arc powers and durations. While the joint region of equal fibers may be optically invisible with optimal settings, the splice point of dissimilar ones is mostly visible as a white colored area [51]. Structural changes in the cladding region may also be seen directly under a microscope. To optimize the splice parameters, the area of discoloration and visible joint region have been reduced to a minimum. Additionally, the losses estimated by the splicer have been lowered to reproducible values well below 0.03 dB.

The optimized parameters with respect to the different fiber combinations are listed in the appendix A.1. To evaluate the success of the splicing procedure, the mode profile and its propagation has to be measured and compared to a Gaussian beam.

## 5.4 Exiting Mode Characterization

After a fiber assembly with single-mode, GRIN and multi-mode fiber has been produced (an example is shown in figure 5.8), it is necessary to characterize its output mode. To ensure high coupling rates, the exiting beam has to be examined for optical aberrations and the conformity with the cavity mode the mirrors are produced for. One way of doing so is to measure the beam radii at different distances from the fiber end-facet with the knife-edge method, as it is presented in [22, 55]. Formula 2.15 is fitted to the obtained radii, whereas the factor  $z$  is replaced by  $z - z_0$ . Then,  $z$  denotes the distance from the fiber tip, from where the radius was determined.  $z_0$  denotes the distance of the waist position from the fiber end. For this measurement, the fiber is placed on a translation stage allowing to move it relative to the knife in steps of 150 nm, whereby its position is internally metered with a resolution of 17.4 nm [56]. The remaining power behind the knife is recorded with a power meter, whereby its measurements are ten times averaged for each data point. The angle of the stage axes with respect to the knife is less than  $0.5^\circ$ , as it is shown in figure 5.9.

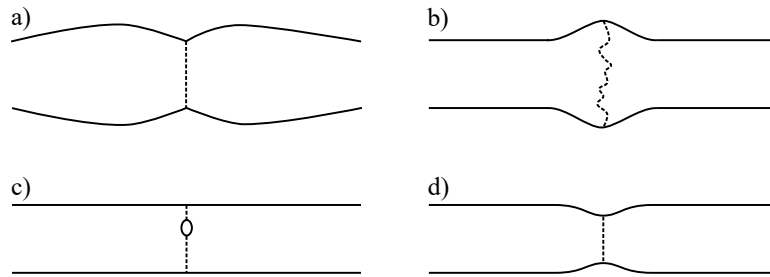


Figure 5.7: In this figure, different shapes of splices with unfavorable arc powers or durations are illustrated.:

- a): If a too long or too powerful pre-fuse heats the fibers such that the region behind the joint is softer than the joint material itself, bulges are formed while pushing the fibers into each other.
- b): Too long or powerful main arc powers can melt the fiber tips so that material liquidifies and forms a bulge. Furthermore, the fiber overlap may be too large that molten glass evades to the side.
- c): Dirt and strong ripples on the fiber tips cause bubbles in the fiber joint. They do not influence the stability of the splice, but may cause significant mode deterioration.
- d): Inadequate power and arc durations may also cause a thin fiber joint.



Figure 5.8: This figure shows a fiber assembly with a 780HP single-mode, a GIF625 GRIN and an FG105LCA multi-mode fiber.

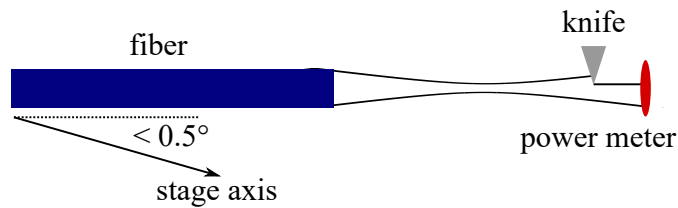


Figure 5.9: In this figure, a sketch of the knife-edge measurement setup is depicted.

In a first step, the output mode of a 780HP fiber with fiber lenses made of the three introduced GRIN fibers were investigated. Since the OFS BF04432-1 sample has shown the strongest deviations from an ideal Gaussian beam propagation, it has not been considered for further steps. The exiting mode of the InfiniCor300 as well as the GIF625 fiber samples looks nearly identical with an ideal Gaussian beam propagation as shown in figure 5.10. Consequently, attempts of producing assemblies with additional multi-mode fiber have been performed with these two fibers. In a further step, assemblies with arbitrary lengths of 380 nm GRIN fiber and 50  $\mu\text{m}$  multi-mode fiber, as it is shown in figure 5.8, were investigated and the results are presented in figure 5.11 .

Although the beam propagations of both fibers follow a Gaussian beam, only the GIF625 shows an aberration-free beam propagation.

In conclusion, the technique of fabricating fiber integrated mode-matching optics is now available to build the next generation of fiber cavities in our facilities.

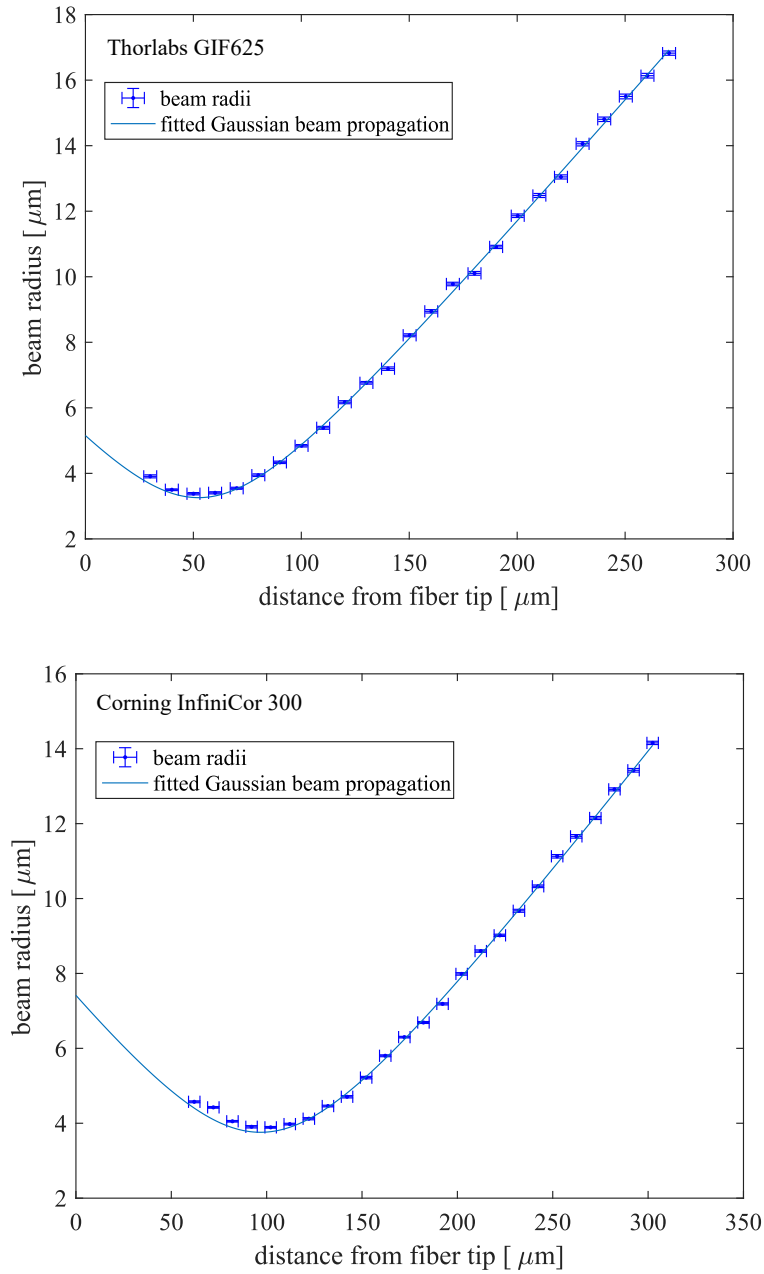


Figure 5.10: Measured output mode of a 780HP single mode fiber equipped with GRIN fiber lenses of 380  $\mu\text{m}$  length made of the Corning InfiniCor and the Thorlabs GIF625 fiber.

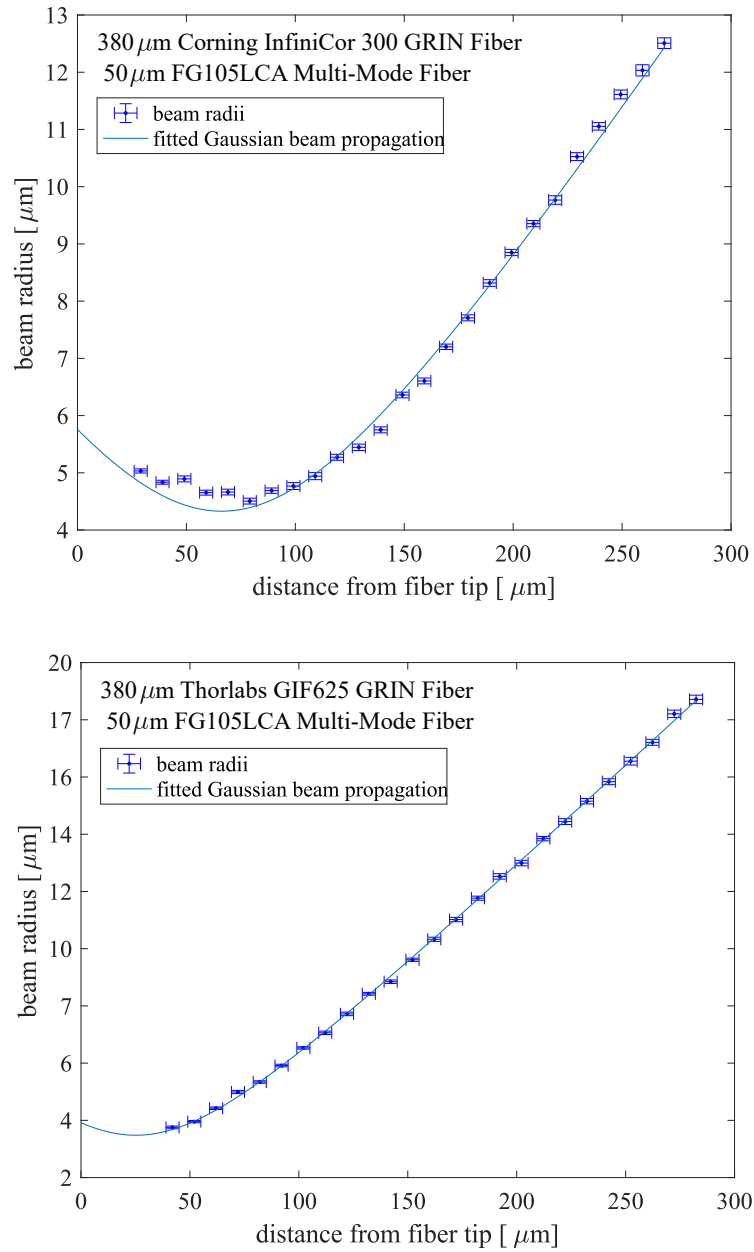


Figure 5.11: This figure shows measured output mode propagations of fiber assemblies made of single-mode, GRIN and multi-mode fibers. The upper beam propagation is measured for a Corning InfiniCor 300 fiber lens of 380  $\mu\text{m}$  length. The lower assembly is equipped with a Thorlabs GIF625 fiber lens of 380  $\mu\text{m}$  length.



---

## Conclusion and Outlook

---

During this thesis, a laser ablation setup for fiber mirror production has been set up (section 3.2). The acquired beam pointing and power stability gives the possibility to apply the dot milling technique (section 3.3). After extensive tests by Pia Fürtjes, it can be concluded that the system works for creating mirrors with a wide range of different geometries (section 3.5). This enables the production of mirrors for large cavities.

The setup is further improved by Moritz Scharfstädt, who implemented a PID controller to actively reduce power fluctuations. It has been detected that regular power fluctuations occur with a repetition time of approximately  $20\ \mu\text{s}$  because of discontinuous pumping of the laser at lower duty cycle [36]. Since the controller would follow these short time fluctuations, they can disturb the feedback process. So, the duty cycle has been set to 100 %, raising the necessity of further attenuation. In addition, a polarization independent partial reflector had to be installed to direct light onto the photodiode, since jumps in polarization of the laser light were observed leading to jumps of the detected power.

Furthermore, a production facility for fiber cavities has been set up (see chapter 4). This includes the mechanical alignment part as well as an optical setup, with which the cavity resonances can be observed continuously (section 4.1). From these measurements, parameters like the coupling efficiency and the finesse can be determined. With this continuous monitoring, the alignment can be optimized during the assembly procedure by improving the coupling to the cavity mode (section 4.3). In order to test this setup, a fully functioning fiber cavity has been produced. Within one day, a completely new cavity system can be assembled, which is suited for the use in the group's FCQED experiment after additional equipping with a lens system. The analysis part has also been used for the bachelor thesis of Hannah Nienhaus and is currently used by Carlos Saveedra to fabricate more robust cavities of the rigid cavity design described in [18].

The problem of the wide distribution of finesse values remained, although the sideband generation has been improved by replacing the AOM by an electro-optical modulator. In the future, another measurement technique can be applied to utilize the interference signal of the reflected electric field in the fiber and the decaying intra-cavity field for ringdown spectroscopy, as presented in reference [57].

Additionally, a vacuum system has been set up, which can be used to investigate the cause of the finesse degradation observed in the FCQED experiment in our research group (see section 4.4). It has still to be equipped with a source for vaporized rubidium to mimic the environment of the FCQED experiment.

In the last part, advanced techniques for realizing mode-matched fiber cavities have been demonstrated (see chapter 5). These include the splicing of single-mode, GRIN and multi-mode fibers without significant beam quality deteriorations (see section 5.3) and micrometer length control in cleaving processes (see section 5.2).

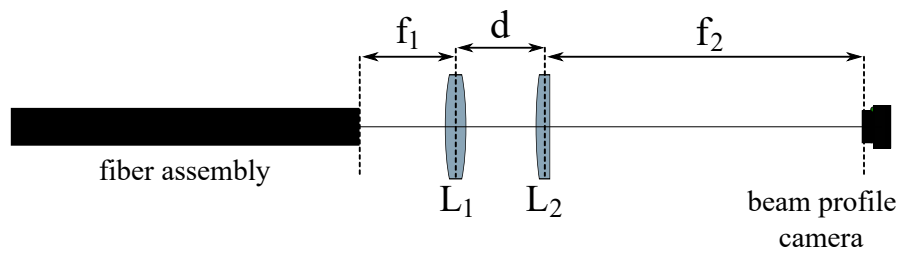


Figure 6.1: This figure illustrates the first attempt to measure a beam propagation with a beam profile camera and a system of lenses magnifying the beam by a factor of 25. To measure a complete propagation, the fiber assembly is pulled backward in steps of  $10\ \mu\text{m}$ . For every step an image is taken, from which the brightness of every pixel is extracted. An elliptic Gaussian function is fitted to the brightness values to determine beam widths and ellipticities.

A knife-edge measurement apparatus has been set up to precisely characterize the output mode. However, this technique has several drawbacks. One disadvantage is the large data acquisition time between 4 h and 15 h. For a volume production of mode-matched fiber cavities, this time has to be lowered to some minutes.

The first attempt to measure the beam propagation has been performed with a microscope setup and a beam profile camera. The beam has to be magnified by a factor of 20, since its original diameter is on the order of one pixel size. As a magnification system an aspheric lens with a focal length of  $f = 20\ \text{mm}$  and a plano-convex lens with  $f = 500\ \text{mm}$  have been used (see figure 6.1). Beam propagations have been measured by imaging the beam at the fiber tip on the camera and then taking images while moving the fiber out of focus. The results showed strong aberrations, most probably originating from spherical aberrations. However, successfully implemented, this measurement technique would have strong advantages. It would speed up the characterization process from many hours to minutes and includes the full two dimensional map of the exiting mode. In a next step, the aspheric lens should be replaced by a suitable microscope objective.

In conclusion, all necessary fabrication, assembly and characterization setups for manufacturing mode-matched fiber Fabry-Perot cavities have been established or improved in our laboratories. A wide range of cavity parameters depending on the envisaged application can now be accessed. These include mode-matched cavities for cavity-QED experiments with neutral atoms, long mode matched cavities for ion-based cavity QED experiments or spectroscopy and mode-matched cavities for efficient, but small footprint optical filters.

# Bibliography

---

- [1] E. M. Purcell, H. C. Torrey and R. V. Pound,  
*Resonance absorption by nuclear magnetic moments in a solid*, Physical Review Letters **69** (1946)  
(cit. on p. 1).
- [2] M. Fox, *Quantum optics: an introduction*, vol. 15, OUP Oxford, 2006 (cit. on pp. 1, 3, 8–10).
- [3] G. Gabrielse, *Observation of inhibited spontaneous emission*,  
Physical Review Letters **55** (1985) 67 (cit. on p. 1).
- [4] J. Gallego et al., *Strong Purcell effect on a neutral atom trapped in an open fiber cavity*,  
arXiv preprint arXiv:1804.08526 (2018) (cit. on p. 1).
- [5] M. Steiner et al., *Single ion coupled to an optical fiber cavity*, Physical Review Letters **110** (2013)  
(cit. on p. 1).
- [6] J. C. Gallego Fernandez,  
*Strong coupling between small atomic ensembles and an open fiber cavity*,  
PhD thesis: Universitäts- und Landesbibliothek Bonn, 2017 (cit. on pp. 1, 10, 23, 28, 29).
- [7] R. Albrecht et al.,  
*Coupling of a single nitrogen-vacancy center in diamond to a fiber-based microcavity*,  
Physical Review Letters **110** (2013) (cit. on p. 1).
- [8] D. Hunger et al., *A fiber Fabry–Perot cavity with high finesse*, New Journal of Physics **12** (2010)  
(cit. on pp. 1, 2, 16).
- [9] Y. Colombe et al.,  
*Strong atom–field coupling for Bose–Einstein condensates in an optical cavity on a chip*,  
Nature **450** (2007) (cit. on p. 1).
- [10] R. J. Barbour et al., *A tunable microcavity*, Journal of Applied Physics **110** (2011) (cit. on p. 1).
- [11] N. E. Flowers-Jacobs et al., “Optomechanics in a Fiber Cavity”, Optical Society of America, 2012  
(cit. on p. 1).
- [12] M. Kohnen et al., *An array of integrated atom-photon junctions*, Nature Photonics **5** (2011)  
(cit. on p. 1).
- [13] P. Horak et al., *Possibility of single-atom detection on a chip*, Physical Review A **67** (2003)  
(cit. on p. 1).
- [14] G. K. Gulati et al., *Fiber cavities with integrated mode matching optics*,  
Scientific Reports **7** (2017) 5556 (cit. on pp. 2, 5, 31, 32).
- [15] M. Uphoff et al.,  
*An integrated quantum repeater at telecom wavelength with single atoms in optical fiber cavities*,  
Applied Physics B **122** (2016) (cit. on p. 2).

- [16] B. Lounis and M. Orrit, *Single-photon sources*, Reports on Progress in Physics **68** (2005) (cit. on p. 2).
- [17] G. Gagliardi and H.-P. Loock, *Cavity-enhanced spectroscopy and sensing*, Springer, 2014 (cit. on pp. 2, 3).
- [18] J. Gallego et al., *High-finesse fiber Fabry-Perot cavities: stabilization and mode matching analysis*, Applied Physics B **122** (2016) (cit. on pp. 3, 13, 14, 27, 43).
- [19] B. Bernhardt et al., *Cavity-enhanced dual-comb spectroscopy*, Nature Photonics **4** (2010) (cit. on p. 3).
- [20] S. Ritter et al., *An elementary quantum network of single atoms in optical cavities*, Nature **484** (2012) (cit. on p. 3).
- [21] B. E. Saleh and M. C. Teich, *Fundamentals of photonics*, vol. 22, Wiley New York, 1991 (cit. on pp. 3, 4).
- [22] M. Kubista, *A New Fiber Mirror Production Setup*, Masterthesis, Rheinische Friedrich-Wilhelms-Universität Bonn (2017) (cit. on pp. 4, 16, 19, 20, 37).
- [23] D. Meschede, *Optics, light and lasers: the practical approach to modern aspects of photonics and laser physics*, Wiley-VCH Verlag GmbH & Co. KGaA, 2006 (cit. on pp. 5, 10).
- [24] C.-k. Ji et al., *Micrometer-resolution in-fiber OCT probe with tunable working distance*, Optics Express **24** (2016) (cit. on p. 5).
- [25] A. Mafi et al., *Low-loss coupling between two single-mode optical fibers with different mode-field diameters using a graded-index multimode optical fiber*, Optics letters **36** (2011) 3596 (cit. on p. 5).
- [26] D. Lorensen, X. Yang and D. D. Sampson, *Accurate modeling and design of graded-index fiber probes for optical coherence tomography using the beam propagation method*, IEEE Photonics Journal **5** (2013) (cit. on pp. 5–8, 32).
- [27] N. Ismail et al., *Fabry-Pérot resonator: spectral line shapes, generic and related Airy distributions, linewidths, finesse, and performance at low or frequency-dependent reflectivity*, Optics Express **24** (2016) (cit. on p. 8).
- [28] W. Demtröder, *Atoms, Molecules, and Photons*, Springer, 2006 (cit. on p. 8).
- [29] K. Ott et al., *Millimeter-long fiber Fabry-Perot cavities*, Optics Express **24** (2016) (cit. on pp. 9, 18, 19).
- [30] R. Paschotta, *Beam quality deterioration of lasers caused by intracavity beam distortions*, Optics Express **14** (2006) (cit. on p. 10).
- [31] M. Uphoff et al., *Frequency splitting of polarization eigenmodes in microscopic Fabry-Perot cavities*, New Journal of Physics **17** (2015) (cit. on pp. 11, 17, 28).
- [32] W. Joyce and B. DeLoach, *Alignment of Gaussian beams*, Applied Optics **23** (1984) (cit. on p. 12).
- [33] B. Brandstätter et al., *Integrated fiber-mirror ion trap for strong ion-cavity coupling*, Review of Scientific Instruments **84** (2013) (cit. on pp. 12, 29).

- 
- [34] C. R. Webster et al., *Isotope Ratios of H, C, and O in CO<sub>2</sub> and H<sub>2</sub>O of the Martian Atmosphere*, *Science* **341** (2013) (cit. on p. 15).
- [35] R. Briggs et al., “Compact Multi-Channel Infrared Laser Absorption Spectrometer for Spacecraft Fire Safety Monitoring”, 46th International Conference on Environmental Systems, 2016 (cit. on p. 15).
- [36] P. Fürtjes, *Integrated Fibre Cavity for Quantum Networks*, Masterthesis, Rheinische Friedrich-Wilhelms-Universität Bonn (2018) (cit. on pp. 15, 17, 18, 22, 33, 43).
- [37] R. Kitamura, L. Pilon and M. Jonasz, *Optical constants of silica glass from extreme ultraviolet to far infrared at near room temperature*, *Applied Optics* **46** (2007) (cit. on p. 15).
- [38] M. Feit and A. Rubenchik, *Modeling of laser induced damage in NIF UV optics*, tech. rep., Lawrence Livermore National Lab., CA (US), 2001 (cit. on p. 16).
- [39] N. Thau, *Optical fiber cavities*, Masterthesis, Rheinische Friedrich-Wilhelms-Universität Bonn (2012) (cit. on p. 16).
- [40] D. Hunger et al., *Laser micro-fabrication of concave, low-roughness features in silica*, *Aip Advances* **2** (2012) (cit. on pp. 16, 18).
- [41] Coherent, *Coherent C55L 9.3 Data Sheet*, (1111) (cit. on p. 16).
- [42] C. Sung, S. Y. Tochitsky and C. Joshi, “Guiding of 10  $\mu$ m laser pulses by use of hollow waveguides”, *AIP Conference Proceedings*, vol. 737, 1, AIP, 2004 (cit. on p. 17).
- [43] S. Garcia et al., *Dual-wavelength fiber Fabry-Perot cavities with engineered birefringence*, arXiv preprint arXiv:1805.04089 (2018) (cit. on p. 19).
- [44] G. Jäger et al., *Nanomeasuring and nanopositioning engineering*, *Measurement* **43** (2010) (cit. on p. 19).
- [45] L. Mingzhou, *Development of fringe analysis technique in white light interferometry for micro-component measurement.*, PhD thesis, 2009 (cit. on p. 20).
- [46] Epoxy Technology, *Epo-Tek 353ND Data Sheet*, (2017), URL: [http://www.epotek.com/site/administrator/components/com\\_products/assets/files/Style\\_Uploads/353ND.pdf](http://www.epotek.com/site/administrator/components/com_products/assets/files/Style_Uploads/353ND.pdf) (cit. on p. 25).
- [47] Epoxy Technology, *Epo-Tek H202E Data Sheet*, (2018), URL: [http://www.epotek.com/site/administrator/components/com\\_products/assets/files/Style\\_Uploads/H20E.pdf](http://www.epotek.com/site/administrator/components/com_products/assets/files/Style_Uploads/H20E.pdf) (cit. on p. 28).
- [48] Epoxy Technology, *Epo-Tek OG116-31 Data Sheet*, (2017), URL: [http://www.epotek.com/site/administrator/components/com\\_products/assets/files/Style\\_Uploads/OG116-31.pdf](http://www.epotek.com/site/administrator/components/com_products/assets/files/Style_Uploads/OG116-31.pdf) (cit. on p. 28).
- [49] D. Gangloff et al., *Preventing and reversing vacuum-induced optical losses in high-finesse tantalum (V) oxide mirror coatings*, *Optics Express* **23** (2015) (cit. on p. 29).
- [50] H. Nienhaus, *Charakterisierung und Temperr optischer Faserspiegel*, Bachelor’s Thesis, 2019 (cit. on p. 29).
- [51] A. D. Yablon, *Optical fiber fusion splicing*, vol. 103, Springer Science & Business Media, 2005 (cit. on pp. 33, 34, 36, 37).

- [52] Fujikura Ltd., *ARCmaster FSM 100 Series Data Sheet*, (2013),  
URL: [https://www.opternus.de/media/pdf/80/0f/42/fsm-100pplus-FSM100\\_db10213de2GSpFwLCoBTLt.pdf](https://www.opternus.de/media/pdf/80/0f/42/fsm-100pplus-FSM100_db10213de2GSpFwLCoBTLt.pdf) (cit. on p. 36).
- [53] A. W. Laubengayer,  
*Germanium XVII.: Fused Germanium Dioxide and Some Germanium Glasses*,  
PhD thesis: Cornell University, 1926 (cit. on p. 36).
- [54] G. Zhang et al.,  
*Interface modification based ultrashort laser microwelding between SiC and fused silica*,  
*Optics Express* **25** (2017) (cit. on p. 36).
- [55] Y. Suzuki and A. Tachibana,  
*Measurement of the  $\mu\text{m}$  sized radius of Gaussian laser beam using the scanning knife-edge*,  
*Applied Optics* **14** (1975) (cit. on p. 37).
- [56] Newport Cooperation, *Newport MFA-CC Linear Stage User's Manual*, (2018) (cit. on p. 37).
- [57] D. Bresteau, C. Blondel and C. Drag,  
*Saturation of the photoneutralization of a H- beam in continuous operation*,  
*Review of Scientific Instruments* **88** (2017) (cit. on p. 43).

## **Useful information**

---

### **A.1 Optimized Splice Parameters**

As it is described in section 5.3.2, suitable splice settings have to be found for every combination of fibers used in this project. The following table lists the optimized parameters:

	780HP – GIF625/InfiniCor	780HP – BF04432-1	FG105LCA – GIF625/InfiniCor
gapset	gap	15 µm	25 µm
	gap-center shift	L – 15 µm	R – 20 µm
cleaning arc	power	STD – 50bit	STD – 50bit
	duration	100 ms	100 ms
prefuse	duration	20 ms	50 ms
	on-time	20 ms	5 ms
	off-time	off	45 ms
	power	STD – 80bit	STD
joint forming	overlap	10 µm	15 µm
			15 µm
main arc	duration	2000 ms	3000 ms
	power	STD – 40bit	STD – 70bit
			2500ms
			STD – 40bit

# List of Figures

---

2.1	This sketch illustrates the structure of fibers with their refractive index profile. The light is guided in the core, which is surrounded by the cladding to create a refractive index transition. Around the fiber, a coating is applied for protection. . . . .	4
2.2	This figure shows ray tracing pictures of modes in a): single-mode fibers, b) multi-mode fibers and c): graded-index fibers. The image is taken from [22]. . . . .	4
2.3	Illustration of positive spherical aberrations of GRIN fiber lenses. . . . .	6
2.4	Illustration of negative spherical aberrations of GRIN fiber lenses. . . . .	7
2.5	Influence of the refractive index dip on the mode propagating in- and outside the fiber sample. . . . .	7
2.6	Prediction and measurement of the beam propagation after a fiber lens from 100/140 MMF POFC GRIN fiber. The prediction without a long ripple is displayed on the left, the one with it is on the right. The image is taken from [26]. . . . .	8
2.7	Definition of incoming, circulating and transmitted power through the cavity. Further, a transmission spectrum through the cavity is shown. . . . .	9
2.8	Cavity transmission spectrum and intensity distribution of higher order transversal modes.	11
2.9	Fundamental Gaussian mode in a cavity. . . . .	12
2.10	This figure illustrates the definition of decentrations of mirror and core (marked in red) $d$ , as well as angles of the mirror with respect to the fiber axis normal $\theta$ . . . . .	13
2.11	This figure illustrates the origin of the asymmetric reflection lineshape of fiber Fabry-Perot cavities. . . . .	14
3.1	Sketch of the new fiber shooting setup. . . . .	17
3.2	This figure shows the beam widths around the waist of the laser beam measured with the knife-edge method. . . . .	18
3.3	Illustration of the dot milling technique. . . . .	19
3.4	Setup of the interference microscope. . . . .	20
3.5	Light paths in a Mirau objective. . . . .	20
3.6	Reconstructed fiber end facet after treatment with the dot milling technique. . . . .	22
4.1	Optical setup for cavity alignment and lineshape observation. . . . .	24
4.2	Electrical circuit for piezo high voltage supply. . . . .	25
4.3	Finesse and cavity resonance width measurement. . . . .	26
4.4	Estimated finesse values for different scan frequencies. . . . .	27
4.5	This figure shows a sketch of the cavity design. The image is adapted from [18]. . . . .	27
4.6	This figure shows the construction of the T-piece (below), the shear piezo (middle) and the V-groove (top), in which the fiber is placed for the cavity assembly. . . . .	28
4.7	This figure shows a sketch of the assembled vacuum system for glue curing. In the future, it can be extended with a rubidium source to investigate the cause of finesse degradations.	29

5.1	This figure shows the approach to install mode-matching optics into fiber cavity assemblies. The laser light is mode cleaned in a single-mode fiber, before its mode is converted by GRIN fiber lens. The mirror is machined onto a piece of multi-mode fiber. . . . .	31
5.2	This figure illustrates structural areas typically arising from unfavorable cleave tensions. The image is adapted from [51]. . . . .	33
5.3	Interferogram of a fiber cleaved while applying a too large force. . . . .	33
5.4	This figure illustrates the cleaver setup for cleave length control. . . . .	34
5.5	This figure illustrates the reproducibility of cleave lengths. Deviations at a given setting are less than 3 $\mu\text{m}$ . . . . .	35
5.6	This figure illustrates the fiber alignment inside the fusion splicer used for this project. Among others the gap between the fibers and the position of the gap center are adjustable. Displacements of the fibers with respect to each other are less than 100 nm. . . . .	37
5.7	Shapes of splices with poor quality due to unfavorable settings. . . . .	38
5.8	This figure shows a fiber assembly with a 780HP single-mode, a GIF625 GRIN and an FG105LCA multi-mode fiber. . . . .	38
5.9	In this figure, a sketch of the knife-edge measurement setup is depicted. . . . .	39
5.10	Measured output mode of a 780HP single mode fiber equipped with GRIN fiber lenses of 380 $\mu\text{m}$ length made of the Corning InfiniCor and the Thorlabs GIF625 fiber. . . . .	40
5.11	This figure shows measured output mode propagations of fiber assemblies made of single-mode, GRIN and multi-mode fibers. The upper beam propagation is measured for a Corning InfiniCor 300 fiber lens of 380 $\mu\text{m}$ length. The lower assembly is equipped with a Thorlabs GIF625 fiber lens of 380 $\mu\text{m}$ length. . . . .	41
6.1	This figure illustrates the first attempt to measure a beam propagation with a beam profile camera and a system of lenses magnifying the beam by a factor of 25. . . . .	44